# nature methods

Article

# Large Stokes shift fluorescent RNAs for dual-emission fluorescence and bioluminescence imaging in live cells

Li Jiang[1,2,3,7], Xin Xie [1,2,7], Ni Su[1,2,7], Dasheng Zhang[1,4,7], Xianjun Chen [1,2,7] ✉, Xiaochen Xu[5,7], Bibi Zhang[1,2], Kaiyi Huang[5,6], Jingwei Yu[1,2], Mengyue Fang[1,2], Bingkun Bao [1,2,3], Fangting Zuo[1,2], Lipeng Yang[1,2,3], Rui Zhang[1,2], Huiwen Li[1,2], Xinyi Huang[1,2,3], Zhengda Chen[1,2], Qingmei Zeng[1,2,3], Renmei Liu[1,2], Qiuning Lin[3], Yuzheng Zhao [1,2], Aiming Ren [5,6] ✉, Linyong Zhu [1,2,3] ✉ & Yi Yang [1,2] ✉

Fluorescent RNAs, aptamers that bind and activate small fluorogenic dyes, have provided a particularly attractive approach to visualizing RNAs in live cells. However, the simultaneous imaging of multiple RNAs remains challenging due to a lack of bright and stable fluorescent RNAs with bio-orthogonality and suitable spectral properties. Here, we develop the Clivias, a series of small, monomeric and stable orange-to-red fluorescent RNAs with large Stokes shifts of up to 108 nm, enabling the simple and robust imaging of RNA with minimal perturbation of the target RNA's localization and functionality. In combination with Pepper fluorescent RNAs, the Clivias enable the single-excitation two-emission dual-color imaging of cellular RNAs and genomic loci. Clivias can also be used to detect RNA–protein interactions by bioluminescent imaging both in live cells and in vivo. We believe that these large Stokes shift fluorescent RNAs will be useful tools for the tracking and quantification of multiple RNAs in diverse biological processes.

Fluorescent proteins have been essential not only for the analysis of protein functions and dynamics but also for the detection of ions, metabolites and protein interactions in live cells and in vivo[1]. Among them, fluorescent proteins with large Stokes shifts (LSS fluorescent proteins) are intriguing tools for the simultaneous imaging of multiple channels, which enables the analysis of multiple biological events or the use of one channel as a reference in quantitative studies[2–6]. This is particularly useful for multiple-photon microscopy, in which multichannel imaging is not easy because of the expense of adding a second titanium–sapphire

(Ti-sapphire) laser or an optical parametric oscillator and the complexity of controlling them together[6]. In addition, because of the large gaps between the excitation and emission wavelengths, LSS fluorescent proteins can serve as efficient acceptors for bioluminescence resonance energy transfer (BRET) from luciferases[4,6], which has been shown to be especially useful in the detection of protein–protein interactions and bioluminescence imaging for in vivo studies[6].

Similar to proteins, RNAs have highly complex distributions, behaviors and functions in cells. A robust fluorescent protein-like

[1]Optogenetics and Synthetic Biology Interdisciplinary Research Center, State Key Laboratory of Bioreactor Engineering, East China University of Science and Technology, Shanghai, China. [2]Shanghai Frontiers Science Center of Optogenetic Techniques for Cell Metabolism, School of Pharmacy, East China University of Science and Technology, Shanghai, China. [3]School of Biomedical Engineering, Shanghai Jiao Tong University, Shanghai, China. [4]Fluorescence Diagnosis (Shanghai) Biotech Company Ltd, Shanghai, China. [5]Life Sciences Institute, Zhejiang University, Hangzhou, China. [6]Department of Orthopedics Surgery, Second Affiliated Hospital, School of Medicine, Zhejiang University, Hangzhou, China. [7]These authors contributed equally: Li Jiang, Xin Xie, Ni Su, Dasheng Zhang, Xianjun Chen, Xiaochen Xu. ✉e-mail: xianjunchen@ecust.edu.cn; aimingren@zju.edu.cn; linyongzhu@ecust.edu.cn; yiyang@ecust.edu.cn

approach for tagging RNAs to monitor RNA dynamics in live cells would be especially useful for understanding their functions and mechanisms underlying diverse biological processes. Fluorescent RNAs, fluorescent protein-like entities consisting of RNA aptamers and corresponding fluorogenic ligands, have provided an attractive approach to visualizing RNAs in live cells. Pioneered by RNA mimics of green fluorescent protein (GFP) such as Spinach and Broccoli[7–9], fluorescent RNAs of different colors from cyan to red have been developed[7–27]. Among them, fluorescent RNAs with enhanced brightness and stability have been successfully used in live cell applications for imaging of RNA and genomic loci, biosensing, and screening. Nevertheless, most of these fluorescent RNAs have Stokes shifts shorter than 40 nm. The only LSS fluorescent RNA available was reported in 2019 by Steinmetzger et al., who induced highly Stokes-shifted emission from HBI (4-hydroxybenzlidene imidazolinone) analogs[28]. However, the use of this LSS fluorescent RNA, named Chili, has not been successful in live cell RNA imaging, probably due to the low quantum yield (<0.1). To date, robust LSS fluorescent RNAs for live cell imaging are highly desirable but as yet have not been developed.

Here, we describe the development of Clivias, a series of small, monomeric and stable orange-to-red fluorescent RNAs with large Stokes shifts of up to 108 nm. We show the usefulness of Clivias in the multicolor imaging of RNA and genomic loci, as well as the detection of RNA–protein interactions both in live cells and in vivo. We believe that these LSS fluorescent RNAs will be useful tools for studying the functionality and mechanisms of RNA underlying diverse biological processes.

## Results

### Development of the small Clivia fluorescent RNAs
We previously designed novel GFP-like, dendritic aromatic acetonitrile-containing fluorophores to strengthen the molecular rigidity and provide firm locking capability for the development of a series of monomeric, highly bright and stable Pepper fluorescent RNAs with a broad range of emission maxima spanning from cyan to red[27,29]. We adapted this approach to the fluorophores of LSS red fluorescent proteins[5,6] and synthesized a new fluorophore, 4-(N-(2-hydroxyethyl)(methyl))benzylidene-3-methyl-2-styryl-3, 5-dihydro-4H-imidazol-4-one, termed NBSI. In NBSI we introduced a dialkylamino group as the electron donor to increase the electron-donating capability, and introduced a styryl group into the molecular skeleton to increase molecular flexibility and intramolecular charge transfer (Fig. 1a), modifications that have been reported to have a strong possibility of increasing the Stokes shifts of fluorophores[30]. NBSI did exhibit a large Stokes shift of 80 nm when it was constrained in glycerol (Extended Data Fig. 1a). We then used SELEX (systematic evolution of ligands by exponential enrichment) to select aptamers that bound to NBSI and identified one aptamer, R8, that could significantly enhance the fluorescence of NBSI in vitro and in *Escherichia coli* cells (Extended Data Fig. 1b–e). We then performed truncation analysis and obtained a minimized aptamer that has a length of only 30 nucleotides but retains the ability to activate the fluorescence of NBSI (Extended Data Fig. 1f–i). Further mutations identified a mutant with improved thermostability (a melting temperature ($T_m$) of 44 °C), which would enable the aptamer to retain higher fluorescence at physiological temperature (37 °C) (Fig. 1b and Extended Data Fig. 1j–l). We termed this RNA aptamer 'Clivia' and its complex with NBSI 'Clivia580', according to its color and emission maximum.

Clivia580 has a well-defined fluorescence profile with an excitation maximum at 524 nm and an emission maximum at 580 nm (Fig. 1c and Supplementary Table 1). In vitro studies showed that Clivia is quite stable with a low dissociation constant for the NBSI fluorophore ($K_d$ is 55 ± 4 nM) (Fig. 1d). More importantly, Clivia580 exhibited an extremely weak dependence on $Mg^{2+}$ (Fig. 1e), which would be beneficial for RNA imaging in mammalian cells, considering the estimated free

intracellular magnesium concentration of 0.25–1.5 mM (ref. 31). Similar to the Peppers, Clivia folds independently of potassium concentration (Extended Data Fig. 1m), suggesting that there is no G-quadruplex in its structure.

Mammalian cells expressing Clivia embedded in a transfer RNA scaffold had robust orange fluorescence upon incubation with NBSI, whereas the control cells transfected with a plasmid carrying the tRNA alone showed minimal background fluorescence, which resulted in a high signal-to-background ratio of ~24-fold (Fig. 1f,g). In comparison, Chili, the only LLS fluorescent RNA reported, had very dim fluorescence when the cells were incubated with DMHBI-lmi, with a ~20-fold weaker brightness than the cells expressing tRNA-Clivia (Fig. 1f,g). No specific fluorescence was observed when the cells were incubated with DMHBO+, another HBI analog that binds to the Chili aptamer with a higher affinity than DMHBI-lmi[28] (Fig. 1f,g). In addition, Clivia's intracellular fluorescence significantly increased with increasing copy number of the aptamer in tandem (Extended Data Fig. 1n–p). These biochemically favorable characteristics make Clivia a promising candidate for tagging functional RNAs inside cells.

### Expanding the spectral range of Clivia fluorescent RNAs
Similar to HBC ((4-((2-hydroxyethyl)(methyl)amino)-benzylidene)-cyanophenylacetonitrile) ligands bound by Pepper RNA, NBSI has a typical chromophore structure consisting of an electron donor and an electron acceptor linked by π conjugation. We envisaged that spectroscopic shifting of NBSI would be achieved by altering the electron donor and electron acceptor to change their electron donating and withdrawing capabilities, respectively. To validate our hypothesis, we first kept the electron donor group unchanged and substituted different electron acceptors on the benzene ring by introducing hydroxyl, fluorine or cyan groups into the para- or meta-position of the benzene ring (Extended Data Fig. 2). The para- or meta-position substitution with hydroxyl or fluorine slightly altered the binding of the fluorophore with Clivia, and also altered the emission spectra of the RNA–fluorophore complexes (Fig. 2a,b and Supplementary Table 1). Notably, the enhanced withdrawing capability of the electron acceptor led to increased Stokes shifts in addition to red-shifted emissions, as predicted. For example, substitutions of cyano groups at the para- and meta-positions resulted in 44 nm and 20 nm red-shifted emissions, respectively (Fig. 2a,b), and NBSI624 (para-position substitution with cyano group) had the largest Stokes shift of 90 nm (Fig. 2b and Supplementary Table 1).

We next replaced the donor group with phenolic hydroxyl and introduced two fluorine residues to keep the fluorophores exclusively in the phenolate form, which has been shown to have a higher extinction coefficient and brightness in the case of EGFP (enhanced GFP)[7] (Extended Data Fig. 2). Intriguingly, many of the newly synthesized fluorophores not only had improved binding capacities but they also had extended Stokes-shifted fluorescence emissions compared with the original fluorophores, with the largest Stokes shift reaching 108 nm (Extended Data Fig. 3a,b and Supplementary Table 1).

All of these NBSI analogs showed specific and robust fluorescence in live cells (Fig. 2c,d and Extended Data Fig. 3c,d) without any significant cytotoxicity, as shown by the cell proliferation and viability assays (Supplementary Fig. 1). Notably, many of the excitations of the RNA–fluorophore complexes were at approximately 490 nm, making them perfectly suited for two-photon microscopy using GFP excitation (Fig. 2c,d and Extended Data Fig. 3c,d). Additionally, the maximum excitation of these RNA–fluorophore complexes is around 500 nm, enabling robust imaging of RNA using a 1,040 nm excitation in two-photon confocal microscopy (Fig. 2c,d and Extended Data Fig. 3c,d). Live cell photostability analysis showed that most of the Clivias had better photostability than Chili-DMHBI-lmi in both single- and two-photon excitation (Extended Data Fig. 4 and Supplementary Fig. 2). In particular, most
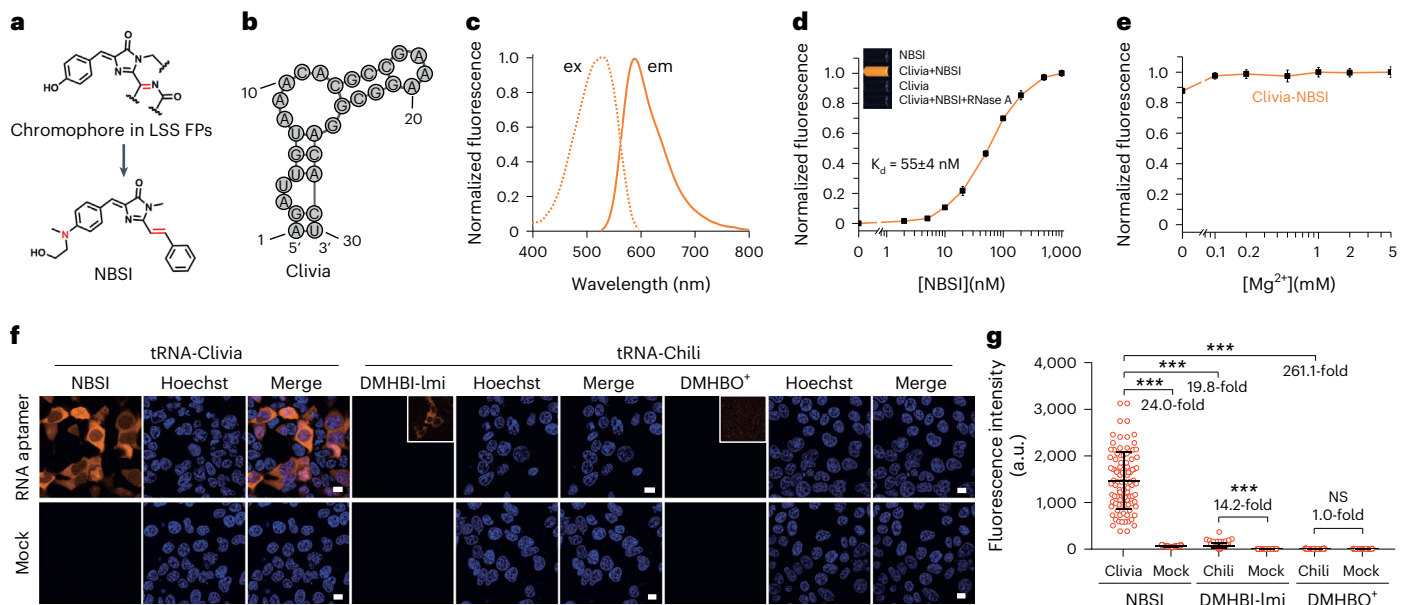
**Fig. 1 | Characterization of Clivia580 fluorescent RNA. a,** Structure of NBSI. An ethylenic bond (red) into the π-conjugation may increase intramolecular charge transfer, thereby resulting in large energy differences between the absorption and emission peaks of the fluorophore. FP, fluorescent protein. **b,** Predicted secondary structure of Clivia. **c,** Excitation (dashed) and emission (solid) spectra of Clivia580. **d,** Clivia580 fluorescence in the presence of increasing concentration of NBSI. Data represent the mean ± s.d. of three biologically independent replicates. **e,** Magnesium dependence of Clivia580. RNA aptamer (1 μM) was mixed with 5 μM NBSI, and the fluorescence signal of the complex was measured with different concentrations of MgCl₂. Data represent the mean ± s.d.

of three biologically independent replicates. **f,** Confocal imaging of live HEK293T cells expressing tRNA-Clivia in the presence of 0.2 μM NBSI, or tRNA-Chili in the presence of 1 μM DMHBI-lmi or DMHBO⁺. HEK293T cells transfected with the empty vector and labeled with the corresponding ligand were used as the controls. The nucleus was stained with Hoechst 33342 (blue). Insets, 20-fold increased contrast. Scale bars, 10 μm. **g,** Quantification of the fluorescence for different RNA–fluorophore complexes in live cells. Statistical analysis was done using a two-tailed t-test. ***$P < 0.001$ versus control; NS, no significant difference. Data represent the mean ± s.d. ($n = 100$ cells).

of the Clivias had even better photostability than the reported LSS fluorescent protein CyOFP1 in two-photon excitation[6] (Supplementary Fig. 2). In this way, we built a series of NBSI analogs that are non-fluorescent in solution but emit bright fluorescence with large Stokes shifts upon binding with Clivia.

Given that many Clivias share excitation spectra similar to those of many Peppers but have large Stokes-shifted emissions, some exceeding 100 nm, they would enable us to carry out single-excitation two-emission dual-color imaging of Clivias and Peppers using single-photon or two-photon microcopy. In vitro studies showed that at concentrations higher than those routinely used for live cell labeling, these two fluorescent RNAs are bio-orthogonal, given that these RNAs only slightly cross-react with one or two of each other's cognate dyes and thus show little cross-activation of their fluorescence (Extended Data Fig. 5a). We then used a protein–RNA tethering system to detect combinations of Clivias and Peppers for dual-color imaging. In this system, we inserted MS2- and boxB-binding hairpins into the terminal stem-loops of Clivia (Clivia-MS2) and Pepper (Pepper-boxB), respectively (Extended Data Fig. 5b,c). The chimeric RNAs were tethered to the outer membranes of the mitochondria and nucleus when co-expressed with N-TOMM20-BFP and tdMCP-SNAP-H2B fusions, respectively (Extended Data Fig. 5c). We found that several combinations of Clivia and Pepper enabled dual-color imaging of two RNAs using single-excitation two-emission fluorescence in single- or two-photon microscopy (Extended Data Fig. 5d,e). Furthermore, we achieved dual-color imaging of U6 small nuclear RNA (snRNA) and *ACTB* messenger RNA in live mammalian cells (Extended Data Fig. 5f). In addition, we also achieved single-molecule mRNA imaging with the tandem array of Clivia in live mammalian cells (Supplementary Fig. 3), demonstrating the potential of Clivia for the imaging of RNA dynamics.

## Imaging of snRNAs tagged with Clivia in live mammalian cells

We noted that the small size of Clivia (30 nucleotides) might open up great opportunities for tagging numerous small non-coding RNAs (ncRNAs) in live cells, whereas large inserts might easily affect the localization and functionality of small ncRNAs. To this end, we fused Clivia to different snRNAs and tested their localizations. As expected, we found that the Clivia fusion with *7SK* snRNA localized to nuclear speckles[32] (Fig. 3a); the Clivia fusion with *U6* splicing RNA or mgU2-47 Cajal body-specific RNA accumulated in Cajal bodies[33,34] (Fig. 3a); and the Clivia fusion with U1 snRNA exhibited sequestration in cytosolic U-bodies containing the marker protein survival motor neuron (SMN) upon treatment with the endoplasmic reticulum stress inducer thapsigargin, consistent with the literature[35] (Fig. 3b). Furthermore, these results were validated by fluorescence in situ hybridization data (Fig. 3a,b) and are consistent with the function and localization of these RNAs. In comparison, cells expressing Chili-tagged ncRNAs showed no specific fluorescence (Fig. 3a,b), probably due to its inherent weak cellular fluorescence or structural instability caused by the interference of snRNAs.

We next studied whether Clivia fusions can be imaged beyond the diffraction limit. For this purpose, we applied structured illumination microscopy (SIM) to image Clivia-tagged U6 and U1. The SIM technique enabled better resolution of the Cajal body and U-body than widefield microscopy, and it seemed that the RNA distribution was more or less non-uniform throughout the granules (Supplementary Fig. 4). Intriguingly, the non-uniform distribution of RNA was also observed in stress granules, with clusters of higher concentration of both RNA and protein in the stress granules[36]. Thus, Clivia-based SIM imaging may be useful in studying the relationship between the structure and functionality of the granules.

We then used Clivia-U1 to monitor U-body induction by thapsigargin, the live cell kinetics of which had not been reported as yet,
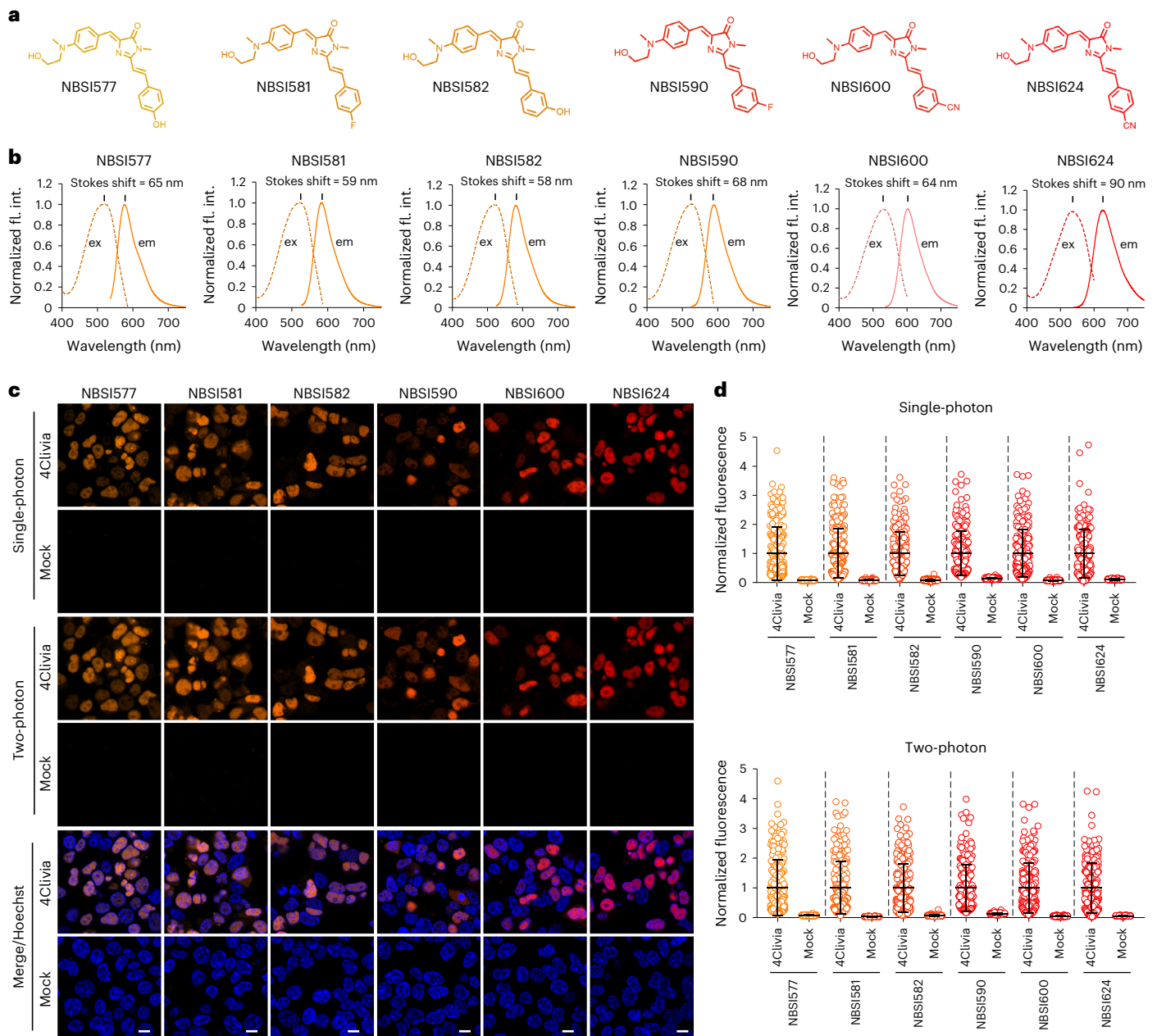
**Fig. 2 | A palette of Clivia fluorescent RNAs with large Stokes shifts. a**, Structures of NBSI analogs. **b**, Excitation (dashed) and emission (solid) spectra of the Clivias and their Stokes shifts. fl. int., fluorescence intensity. **c**, Imaging of HEK293T cells expressing 4Clivia and incubated with 0.2 µM various NBSI analogs. Cells transfected with the empty vector were used as controls. The nucleus was stained with 1 µg ml⁻¹ Hoechst 33342 (blue). Scale bars, 10 µm. **d**, Quantification of the fluorescence for different RNA–fluorophore complexes in live cells. The data were normalized to the average fluorescence of each RNA–fluorophore complex, respectively. Data represent the mean ± s.d. ($n = 200$ cells).

to our knowledge. We performed multiplexed imaging of the time course of the U-body by co-expressing GFP-SMN1 with Clivia-U1 in HEK293T cells, and found that the SMN1 and U1 signals appeared at the same time-frame in the newly formed granules approximately 20 min after thapsigargin treatment (Fig. 3c and Supplementary Video 1). These data support the hypothesis that the U-body represents liquid–liquid phase separation (LLPS), in which high concentrations of assembly components reach a critical threshold and then spontaneously assemble into ribonucleoprotein (RNP) granules through weak multivalent interactions. A similar mechanism was previously shown in the model of stress granule formation[36]. In statistical analysis, the majority of the U-body-containing cells formed the puncta during 0.5–3.0 h after thapsigargin treatment (Fig. 3c,d), and the number of puncta increased first and then slightly decreased with time, probably

due to the fusion of small U-bodies to form large ones (Fig. 3e, Extended Data Fig. 6 and Supplementary Video 2). Intriguingly, we found that these induced U-bodies remained stable after thapsigargin withdrawal, however, they disappeared or became much smaller after the cells entered mitosis (Supplementary Fig. 5). Such previously unknown phenomena highlight the re-organization of RNA stress granules during mitosis, and further investigation is needed into the underlying mechanism. In summary, Clivia is a very suitable RNA tag for studying the spatiotemporal dynamic distributions of small ncRNAs in live cells.
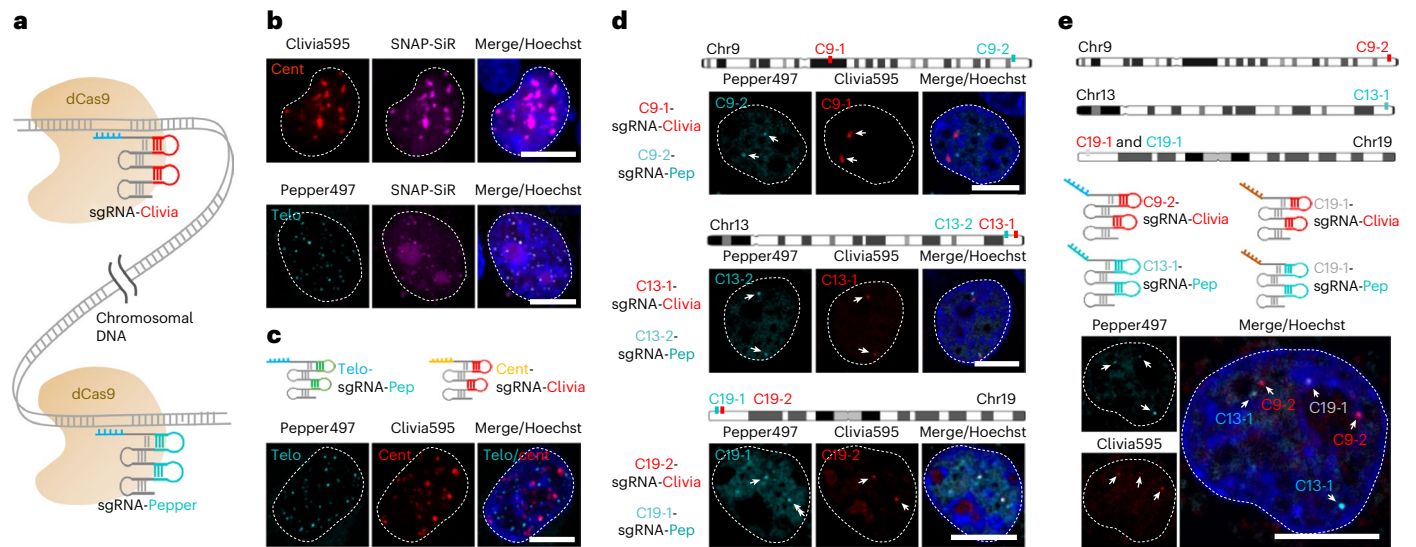
**Dual-color imaging of genomic foci using Clivia and Pepper**
We next performed multiplexed imaging of genomic loci by fusing Clivia and Pepper tandem arrays to the tetraloop of single guide RNA (sgRNA) (Fig. 4a). The cells co-expressing dCas9-SNAP and a Clivia-tagged
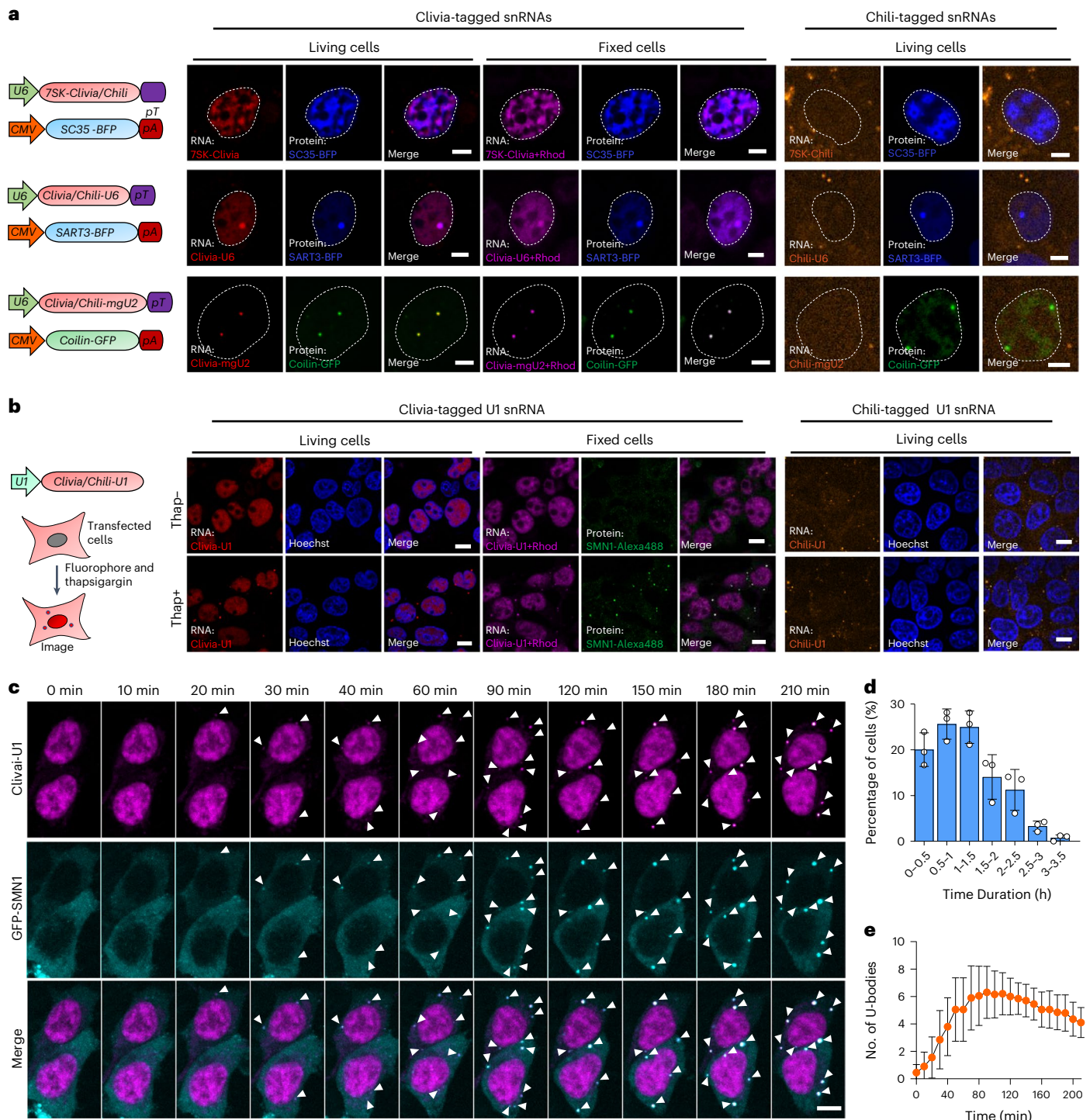
**Fig. 3 | Imaging of snRNAs tagged with Clivia in live mammalian cells.**
**a**, Imaging of snRNA 7SK, U6 and mgU2-47 RNA tagged with Clivia and Chili in the presence of 1 μM NBSI618 and 1 μM DMHBI-lmi, respectively. The HEK293T cells were co-transfected with SC35-BFP, SART3-BFP and Coilin-GFP, respectively. SC35-BFP is used to label nuclear speckles, and SART3-BFP and Coilin-GFP are used to label Cajal bodies. CMV, promoter from human cytomegalovirus; pA, polyadenylation termination signal; pT, poly-T termination signal. Scale bars, 5 μm. **b**, Imaging of HEK293T cells expressing Clivia-U1 or Chili-U1 upon treatment with or without 10 μM thapsigargin (Thap). After transient transfection of Clivia-U1 or Chili-U1, U-bodies were induced by thapsigargin treatment and imaged. For the fixed cells, U1 snRNA was visualized via the fluorescence in situ hybridization probe conjugated with Rhodamine dye,

and endogenous SMN1 was detected by immunofluorescence via antibody conjugated with Alexa488 dye. Scale bars, 10 μm. **c**, Real-time monitoring of U-body puncta formation after thapsigargin induction. HEK293T cells co-expressing Clivia-U1 and GFP-SMN1 were treated with thapsigargin, and consecutive imaging of Clivia and GFP fluorescence was done every 10 min. The U-body puncta are indicated by the white arrowheads. Scale bar, 10 μm. **d**, Duration of puncta formation after thapsigargin induction. Data represent the mean ± s.d. of three biologically independent replicates. **e**, Quantification of the number of U-bodies per cell after thapsigargin induction. Data represent the mean ± s.d. (n = 20 cells). For **a** and **b**, at least two independent experiments were carried out with similar results.

**Fig. 4 | Single-excitation two-emission dual-color imaging of genomic loci.**
**a**, Schematic diagram of the fluorescent RNA-based two-color CRISPR labeling strategy. The Clivia and Pepper aptamers are colored red and cyan, respectively. **b**, Imaging of human centromeric satellites and telomeres using Clivia- and Pepper-tagged sgRNA scaffolds in HEK293T cells, respectively. The nucleus was stained with 1 µg ml⁻¹ Hoechst 33342 (blue). Scale bars, 10 µm. **c**, Simultaneous imaging of human centromeric satellites and telomeres using Clivia- and Pepper-tagged sgRNA scaffolds in HEK293T cells, respectively. The nucleus was stained

with 1 µg ml⁻¹ Hoechst 33342 (blue). Scale bar, 10 µm. **d**, Dual-color imaging of two genomic loci on the same chromosome, C9-1 and C9-2 on chromosome 9, C13-1 and C13-2 on chromosome 13, and C19-1 and C19-2 on chromosome 19. White arrows indicate the corresponding genomic loci. Scale bars, 10 µm. **e**, Simultaneous analysis of three genomic loci using Clivia and Pepper-tagged sgRNA scaffold combinations. White arrows indicate the corresponding genomic loci. Scale bar, 10 µm. For **b**–**e**, at least two independent experiments were carried out with similar results.

centromere-targeting sgRNA or a Pepper-tagged telomere-targeting sgRNA had ~40 red fluorescent puncta of Clivia595 and ~80 green fluorescent puncta of Pepper497, respectively, at centromeric and telomeric loci that perfectly colocalized with SNAP-SiR fluorescence (Fig. 4b and Supplementary Fig. 6), consistent with previous studies[37,38]. When the dCas9 protein was co-expressed together with both chimeric sgRNAs and labeled with NBSI595 and HBC497, the cells showed both green and red fluorescent puncta (Fig. 4c), demonstrating that Clivia and Pepper can be used for the dual-color imaging of multiple genomic loci. Intriguingly, the fluorescent RNA-tagged sgRNA could also be used to derive the approximate copy number of the repeat genomic locus in live cells. The copy number of the telomere sequence (TTAGGG) at each end of each chromosome varied from 205 to 2,017, with an average telomere length of ~4 kilobases (kb) at each end of each chromosome in HEK293T cells (Extended Data Fig. 7), consistent with previous data obtained using quantitative polymerase chain reaction[39].

We next explored the applications of this dual-color system for labeling different repeated chromosome-specific sequences, which would enable assessment of the interchromosomal or intrachromosomal spatial relationships between such loci. We targeted Clivia- and Pepper-tagged sgRNAs to C9-1 and C9-2 on chromosome 9, C13-1 and C13-2 on chromosome 13, and C19-2 and C19-1 on chromosome 19, respectively (Fig. 4d). We observed two specific foci with distinct cytological distances of ~4 µm, ~0.65 µm and ~0.13 µm, corresponding to their known distances of 75 megabase pairs (Mbp), 1.9 Mbp and 4.5 kb between each paired focus on the physical map of the chromosome, respectively (Fig. 4d and Supplementary Fig. 7a). By calculating the genomic locus on the homologous chromosomes, the average intrachromosomal distances for these genomic loci varied from 5.21 µm to 8.58 µm (Supplementary Fig. 7b). In particular, a much closer proximity of the two signals was observed for C19-1 and C19-2, which lie only 4.5 kb apart, with an ~40% overlapping zone at the interface (the white zone in 'Merge') (Fig. 4d and Supplementary Fig. 7c). Notably, C19-1 and C19-2 have only 36 and 45 copies on chromosome 19, respectively, which is significantly lower than the thousands of copies of the centromere and telomere, demonstrating that the multicolor labeling of

low-repeat-containing genomic loci is feasible with our fluorescent RNA-based CRISPR display, thus eliminating the need to pool multiple sgRNAs to achieve sufficient fluorescent signal. Furthermore, multiplexed imaging of telomeres located in all of the chromosomes and C9-1 located only in chromosome 9 enabled us to determine the copy number of chromosome 9 as well as to measure the telomere status by counting the fluorescent puncta and measuring their fluorescence intensities simultaneously (Supplementary Fig. 8). These data indicate that multiplexed imaging with fluorescent RNA-tagged sgRNAs can be used to count specific chromosome copy numbers and/or aberrations. In addition, real-time monitoring of the motion of different chromosomal loci could also be achieved (Supplementary Fig. 9a–e and Supplementary Video 3). However, we did not observe a significant difference in the total motion distances between C13-1 and C9-2 during the 5 min of imaging (Supplementary Fig. 9f). We next explored the possibility of the simultaneous labeling of three different loci by introducing four chimeric sgRNAs into HEK293T cells (Fig. 4e). The locations of the C9-2, C13-1 and C19-1 chromosomal sites could be resolved by their expected colors in live cells: red for C9-2, green for C13-1, and white for C19-1 (merged color of red and cyan) (Fig. 4e). Thus, we can provide a robust and simple methodology for displaying fluorescent RNA in the CRISPR system to simultaneously image multiple endogenous genomic loci in live cells.

## Detection of protein–RNA interactions by bioluminescent imaging

We noted that Clivias have ideal spectral characteristics to serve as a BRET acceptor for NanoLuc (NLuc), a small (19 kDa) luciferase derived from a deep-sea shrimp that uses its substrate to produce blue light (spectral maximum 460 nm)[40], which overlaps substantially with the absorption spectra of the Clivias (Fig. 5a and Supplementary Table 1). If a Clivia and NLuc are in close proximity, the excited-state energy of the oxidized reaction intermediate in the NLuc active site could be transferred to excite Clivia by BRET, leading to emission with the spectrum and quantum yield of the Clivia, which may provide a novel method for the real-time detection of RNA–protein interactions.
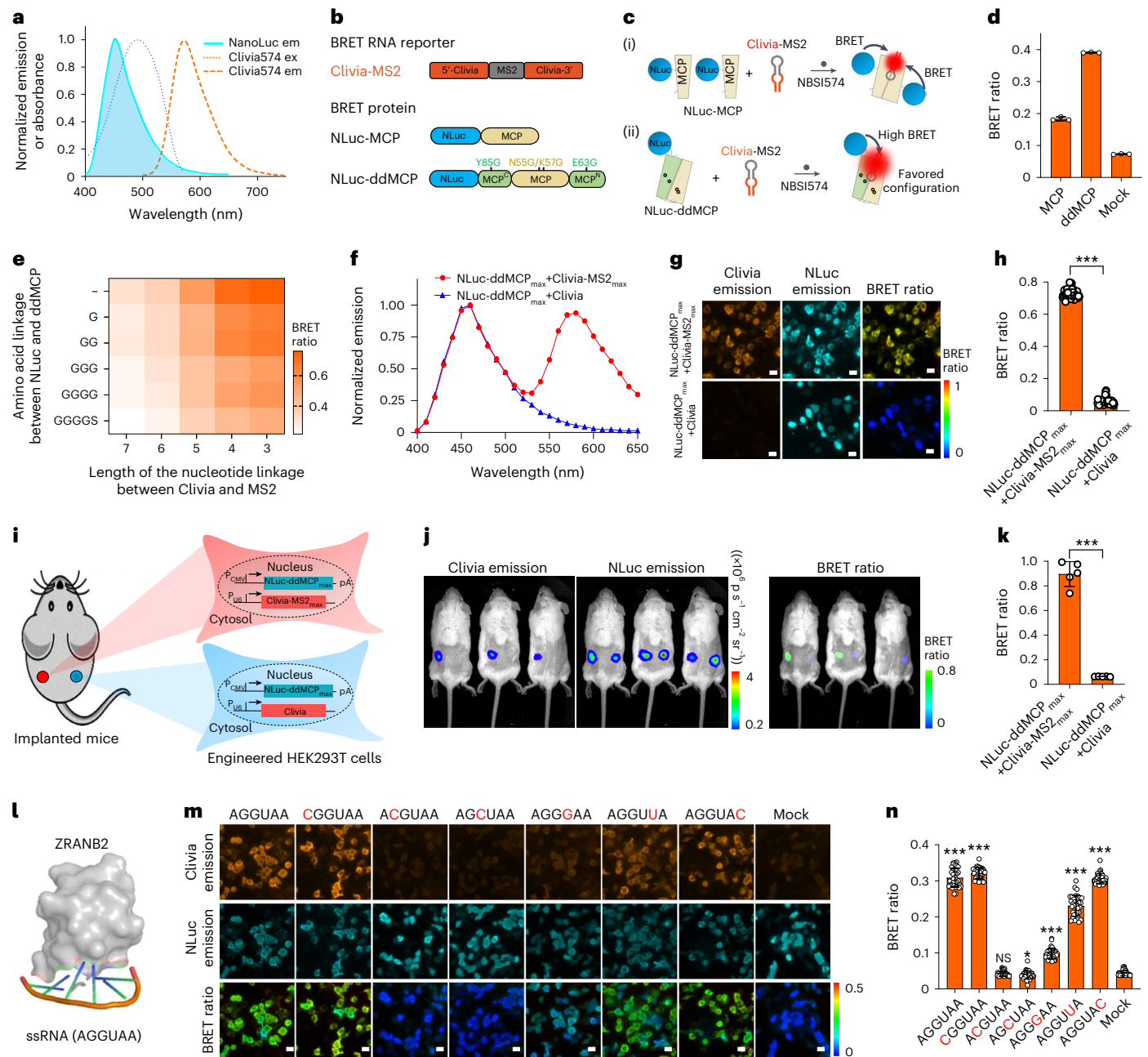
**Fig. 5 | Detection of RNA–protein interactions by bioluminescent imaging.**
**a**, The spectra of the emission of NLuc and the excitation and emission of Clivia574. **b**, Schematic representation of the RNA reporter and BRET fusion proteins. **c**, Schematic representation of the binding models of different BRET fusion proteins to Clivia-MS2 reporter RNA. **d**, BRET efficiency for different BRET fusion proteins. The ratio of light intensity at the emission maximum of Clivia to that of NLuc was calculated. Cells expressing Clivia-MS2 and NLuc without fusion with MCP were used as the controls. Data represent the mean ± s.d. of three biologically independent samples. **e**, Proximity-dependent BRET efficiency for NLuc-ddMCP and Clivia-MS2 containing linkers of different lengths between NLuc and ddMCP and Clivia and MS2. **f,g**, Emission spectra (**f**) and imaging (**g**) of HEK293T cells expressing Clivia-MS2$_{max}$ and NLuc-ddMCP$_{max}$ upon incubation with 1 μM NBSI574 and 10 μM furimazine. Cells expressing Clivia and NLuc-ddMCP$_{max}$ were used as the controls. Data were normalized to the maximum emission. Scale bars, 10 μm. **h**, BRET efficiency of the cells in **g**. Data represent the mean ± s.d. ($n = 50$ cells). **i**, Schematic representation of the dorsal subcutaneous implantation of the engineered HEK293T cells expressing Clivia-MS2$_{max}$ and NLuc-ddMCP$_{max}$. **j,k**, Imaging of the transplanted mice using both Clivia and NLuc emissions after in situ injection of 20 μM furimazine (**j**), and the calculated BRET ratios (**k**). Data represent the mean ± s.d. ($n = 5$ mice). **l**, Schematic representation of the interaction between the ZnF domain of ZRANB2 and an AGGUAA ssRNA motif. **m**, Imaging of the ZRANB2$_{ZnF}$–AGGUAA interaction in live cells. Cells expressing ZRANB2$_{ZnF}$–NLuc and Clivia were used as the controls. Scale bars, 10 μm. **n**, BRET efficiency of the cells in **m**. Data represent the mean ± s.d. ($n = 35$ cells). Statistical comparison in **h**, **k** and **n** was done using a two-tailed t-test. *$P < 0.05$, ***$P < 0.001$ versus controls; NS, no significant difference.

We first used the well-studied MCP–MS2 interaction[41] as a preliminary proof-of-principle demonstration of the utility of Clivia for the detection of RNA–protein interactions (Extended Data Fig. 8a). We inserted the MS2 hairpin RNA into the terminal stem-loop of Clivia as the reporter RNA (Clivia-MS2) and fused NLuc to the MCP coat protein to obtain the NLuc–MCP fusion protein (Fig. 5b,c and Extended Data Fig. 8b). In HEK293T cells expressing Clivia-MS2 and NLuc–MCP, we observed marked emission of Clivia574 and a significantly increased BRET ratio (defined as the ratio of light intensity at the emission maximum of Clivia to that of NLuc) upon incubation with furimazine

compared with the control cells expressing Clivia-MS2 and NLuc (Fig. 5d and Extended Data Fig. 8c), indicating the interaction between the MS2 RNA and MCP protein. Further study showed that the circularly permutated variant of MCP (cpMCP) led to higher BRET efficiency in live cells (Extended Data Fig. 8b,c). Considering that the MCP dimer bound asymmetrically with a single MS2 hairpin RNA[42], and the efficiency of BRET depended on the orientation and relative distance of donor and acceptor dipoles[6], we reasoned that the two NLuc domains in the NLuc–MCP or NLuc–cpMCP dimer might have distinct contributions to the BRET effect (Extended Data Fig. 8d). To this end, we fused NLuc to dMCP, the circularly permuted tandem dimer of MCP, and generated configuration-specific mutants by differentially mutating the amino acids responsible for MS2 binding in each of the MCP domains (Extended Data Fig. 8b,c). We found that the NLuc–dMCP variant carrying E63G/Y85G in the cpMCP domain and N55G/K57G in the MCP domain had the highest BRET efficiency (Fig. 5b–d and Extended Data Fig. 8d,e). We thus termed this dMCP variant 'ddMCP' (directed dMCP) and used it in subsequent studies. As predicted, the NLuc–dMCP variant carrying N55G/K57G in the cpMCP domain and E63G/Y85G in the MCP domain resulted in a markedly decreased BRET ratio even lower than that of dMCP (Extended Data Fig. 8f–h), indicating that this variant binds with MS2 mainly in the unfavored configuration with less efficient BRET. Unlike the structure-based analysis that requires preparation of RNA and protein, the BRET-based mutational analysis enables detection of RNA–protein interaction in live cells, providing a more efficient and convenient way to study the configuration of RNA and protein in the RNA–protein complex.

We next studied the effect of the relative distance of NLuc and Clivia574 dipoles on BRET efficiency by changing the length of the amino acid linkage between NLuc and ddMCP as well as the length of the nucleotide linkage between Clivia and MS2 (Extended Data Fig. 8i,j). Of these combinations, NLuc–ddMCP with no amino acid linkage between NLuc and ddMCP, and Clivia-MS2 with a 3 bp nucleotide linkage between Clivia and MS2 had the highest BRET ratio, and were named NLuc–ddMCP$_{max}$ and Clivia-MS2$_{max}$, respectively (Fig. 5e–h). Notably, fusion of Clivia to the 5′ or 3′ terminus of MS2 hairpin RNA and insertion of Clivia-MS2$_{max}$ into the 3′ terminus of 7SL long non-coding RNA (lncRNA) also produced significant BRET signals in the cells co-expressing the fusion RNA and NLuc–ddMCP$_{max}$ (Supplementary Fig. 10), providing versatile options for creating chimeric reporter RNA for detection of RNA–protein interaction. We found that NBSI analogs could also be used to detect RNA–protein interactions in live cells, with a maximal Clivia emission of >620 nm (Supplementary Fig. 11). As a preliminary proof-of-principle demonstration, we performed dorsal subcutaneous transplantation of engineered HEK293T cells expressing NLuc–ddMCP$_{max}$ and Clivia-MS2$_{max}$ or Clivia (Fig. 5i). After in situ injection of furimazine, we observed marked BRET signals only in the left dorsal subcutaneous transplantation of the cells expressing NLuc–ddMCP$_{max}$ and Clivia-MS2$_{max}$ but not in the right dorsal subcutaneous transplantation of the control cells expressing NLuc–ddMCP$_{max}$ and Clivia (Fig. 5j,k). These data demonstrate that the NLuc–ddMCP$_{max}$ and Clivia-MS2$_{max}$ combination also provides a good opportunity for reporting on RNA dynamics in deep tissues. We thus named the Clivia-MS2$_{max}$ and NLuc–ddMCP$_{max}$-based bioluminescence system the CLUC RNA-lantern system.

Further studies showed that Clivia could also be applied to detect other well-known $\lambda_N$-boxB interactions[43] in live cells (Supplementary Fig. 12). We next asked whether Clivia could be used to detect the inherent RNA–protein interaction in live cells. ZRANB2, containing two zinc finger (ZnF) domains that can recognize an AGGUAA single-stranded RNA (ssRNA) motif with high affinity and specificity, is a widely expressed and highly conserved RS-domain protein that regulates alternative splicing via direct interaction with pre-mRNA[44] (Fig. 5l). To test the ZRANB2–ssRNA interaction, we fused NLuc to the ZnF domain of ZRANB2 (ZRANB2$_{ZnF}$) and fused Clivia to the ssRNA motif

(Fig. 5l). HEK293T cells expressing NLuc–ZRANB2$_{ZnF}$ and Clivia-ssRNA produced a bright Clivia574 signal upon incubation with furimazine (Fig. 5m,n), indicating interaction between ZRANB2$_{ZnF}$ and ssRNA in live cells. Variants of ssRNA with decreased binding affinity with ZRANB2$_{ZnF}$ did have lower BRET efficiencies, consistent with previous studies showing that mutations in the ssRNA motif could alter its binding capacity with ZRANB2$_{ZnF}$ (ref. 44) (Fig. 5m,n). Furthermore, Clivia succeeded in the detection of many other RNA–protein interactions in live cells (Supplementary Fig. 13), by simply fusing the NLuc at the amino or carboxy terminus or the inner of the RBPs according to the structural information of the RNA–RBP complexes, without systematic optimization of the fusion proteins.

We next tested whether the Clivia-based BRET system can be used for understanding more physiologically relevant RNA–protein interactions. Here, we performed detailed BRET-based proximity assay of interaction between U1 snRNA and U1-70K in live cells[45]. We first studied the proximity between different motifs of U1 snRNA and U1-70K. It is known that stem-loop 1 (SL1) of U1 snRNA interacts with U1-70K (ref. 46) (Extended Data Fig. 9a). We inserted Clivia into the other three stem-loops of U1 snRNA and fused NLuc to the RNA binding domain (amino acids 1–194) of U1-70K (Extended Data Fig. 9a,b). Imaging results showed that Clivia insertion had minimal interference with the localization and functionality of U1 snRNA (Extended Data Fig. 9c). In a live cell BRET assay, cells expressing Clivia-U1-SL3 had the highest BRET ratio compared with cells expressing Clivia-U1-SL2 or Clivia-U1-SL4 (Extended Data Fig. 9d,e), consistent with previous reports that SL3 was in closer proximity to the RRM motif of U1-70K than SL2 and SL4 (ref. 45). Therefore, the Clivia-based BRET system not only enables detection of RNA–protein interaction, but also can be used to study the conformational distance between the RNA and protein.

We then studied the contribution of different U1-70K motifs to its interaction with U1 snRNA through BRET imaging and truncation analysis (Extended Data Fig. 10a). Although the structures of U1 snRNP are available[45], which show that the RRM (amino acids 90–194) and α-helix (amino acids 61–89) motifs of U1-70K interact with SL1 of U1 snRNA, the interaction between and proximity of U1-70K and U1 snRNA has not been investigated in live cells, to our knowledge. According to U1 snRNP structures, the tail motif (amino acids 1–60) of U1-70K does not bind with U1 snRNA, instead, it binds with the Sm core's perimeter at two opposite sides to promote the assembly of Sm core[45]. Intriguingly, our data showed that the BRET signal was markedly reduced when the tail motif was truncated, highlighting its important role in stabilizing the binding between U1-70K and U1 snRNA (Extended Data Fig. 10b–d). Further truncation of the a-helix motif completely blocked the U1-70K and U1 snRNA interaction in live cells as shown by the BRET assays (Extended Data Fig. 10c,d), suggesting that the RRM motif alone is not sufficient to support U1-70K and U1 snRNA binding in live cells. Moreover, we found that there was no significant difference in the BRET signals in the U-bodies and in nucleoplasm, or in the BRET signals in non-mitotic and mitotic cells (Extended Data Fig. 10e–h). This indicates that the assembly of U1 snRNP either in the cytoplasm or in the nucleoplasm may be stable, and is not affected by the overcrowded environment in U-bodies or by the sudden mixing of numerous nuclear and cytosolic biological macromolecules during mitosis.

## Discussion

Similar to fluorescent proteins, fluorescent RNAs are emerging and promising tools for the labeling and tracking of RNAs in live cells due to their high modularity and minimal perturbation to the target RNA, which are essential for the deep understanding of mechanisms underlying RNA dynamics and functions. Despite the availability of several fluorescent RNAs that work in live cells[7–27], the simultaneous imaging of multiple RNAs still requires the development of fluorescent RNAs with novel spectral properties and bio-orthogonality. To this end, LSS fluorescent RNAs would be ideal for multiplex RNA tracking and sensor

development. The Clivia fluorescent RNAs developed in this study are not only more stable and brighter than established fluorescent RNAs, they also have larger Stokes shifts. In addition, the Clivia fluorophores, NBSI and its analogs, exhibit low background fluorescence, good membrane permeability and low cytotoxicity, which are favorable characteristics for live cell RNA labeling and imaging. Clivia fluorescent RNAs provide bright signals when co-excited with Pepper fluorescent RNAs, enabling what is to our knowledge multiplex RNA imaging in live mammalian cells without using two lasers in one-photon microscopy or an expensive optical parametric oscillator in two-photon microscopy[12,47]. Using a single-wavelength excitation can significantly reduce image acquisition time and phototoxicity, and provide a better opportunity for faster or more extended study of multiple processes[2,4–6]. Meanwhile, multiplexed imaging with single laser excitation also lowered the cost of instrument investment, which is particularly important for two-photon microcopy or axially swept light-sheet microscopy[2,4–6]. While Clivias are still excited by blue or green light, their emission spectra, which range from orange to red, are of particular interest for live cell imaging because in this spectral range, light is less phototoxic, cellular autofluorescence is reduced, and light-scattering intensity drops off, thereby enabling greater imaging depth and providing great potential for the imaging of RNAs in tissues[48]. These advantages enable Clivias to be especially useful in real-time tracking and monitoring of RNA distributions and dynamics in RNA granules, multiplexed imaging of genomic loci, as well as the detection of RNA–protein interactions in live cells (Supplementary Note 1).

Here, Clivias have been successfully used for visualizing several ncRNAs with relatively high abundance in live cells. However, considering the moderate in vitro brightness (extinction coefficients <30,000 $M^{-1}$ $cm^{-1}$ and quantum yields <0.5) for most Clivias, the use of Clivias to image RNA with very low abundance might be challenging and should be carefully investigated. We have shown here that the tandem arrays of multiple Clivia possess much higher brightness and can be used for single-molecule RNA imaging, which might provide a successful way to improve the fluorescence signal of Clivia-tagged low-abundance RNA. In the future, detailed structural information on the Clivias would help us to understand the photophysics underlying these new RNA–fluorophore complexes, which may facilitate the development of novel LSS fluorescent RNAs with higher brightness and stability.

Various non-membrane-bound cellular compartments, termed RNP granules, have been identified and studied, for example processing body (P-body), stress granule and U-body[49]. Of these, the stress granule is the most extensively studied RNP granule. It is highly dynamic and exhibits ATP-dependent assembly, disassembly, movement, fusion, and fission[36]. Unlike that for stress granules, however, the knowledge on U-bodies is very limited. In this study, we successfully used Clivia-tagged U1 snRNA to visualize the dynamics of U-bodies in live cells upon pharmacological treatment. Similarly to stress granules, the RNA distributions in U-bodies are non-uniform, with clusters of higher concentration of U1 snRNA, and when high concentrations of assembly components (RNA and protein) reach a critical threshold they spontaneously assemble into RNP granules. During the assembly of U-bodies, multiple small granules can fuse with each other to form large granules. Intriguingly, the induced U-bodies disappear or become much smaller after the cells enter mitosis, highlighting the re-organization of U-bodies during mitosis. Although these interesting phenomena have been observed, the underlying mechanisms and connections with biological functions need to be further investigated. In the future, more studies on the dynamics of U-bodies may not only deepen our understanding of RNP granules but also provide fundamental new insights into human disease.

In summary, the Clivias developed here fulfill the requirements for LSS fluorescent RNAs for multicolor imaging of RNA using single-wavelength excitation in mammalian cells. In the future, it would be possible to develop novel LSS fluorescent RNAs based on other state-of-the-art fluorophores with favorable properties, suitable spectra and orthogonality to existing fluorescent RNAs, and use them for multiplexed RNA imaging to explore the functionality and mechanism of multiple RNAs underlying diverse biological processes.

## Online content

Any methods, additional references, Nature Portfolio reporting summaries, source data, extended data, supplementary information, acknowledgements, peer review information; details of author contributions and competing interests; and statements of data and code availability are available at https://doi.org/10.1038/s41592-023-01997-7.

## References

1. Enterina, J. R., Wu, L. & Campbell, R. E. Emerging fluorescent protein technologies. *Curr. Opin. Chem. Biol.* **27**, 10–17 (2015).
2. Shcherbakova, D. M., Hink, M. A., Joosen, L., Gadella, T. W. & Verkhusha, V. V. An orange fluorescent protein with a large Stokes shift for single-excitation multicolor FCCS and FRET imaging. *J. Am. Chem. Soc.* **134**, 7913–7923 (2012).
3. Kogure, T. et al. A fluorescent variant of a protein from the stony coral *Montipora* facilitates dual-color single-laser fluorescence cross-correlation spectroscopy. *Nat. Biotechnol.* **24**, 577–581 (2006).
4. Yang, J. et al. mBeRFP, an improved large Stokes shift red fluorescent protein. *PLoS One* **8**, e64849 (2013).
5. Piatkevich, K. D. et al. Monomeric red fluorescent proteins with a large Stokes shift. *Proc. Natl Acad. Sci. USA* **107**, 5369–5374 (2010).
6. Chu, J. et al. A bright cyan-excitable orange fluorescent protein facilitates dual-emission microscopy and enhances bioluminescence imaging in vivo. *Nat. Biotechnol.* **34**, 760–767 (2016).
7. Paige, J. S., Wu, K. Y. & Jaffrey, S. R. RNA mimics of green fluorescent protein. *Science* **333**, 642–646 (2011).
8. Strack, R. L., Disney, M. D. & Jaffrey, S. R. A superfolding Spinach2 reveals the dynamic nature of trinucleotide repeat-containing RNA. *Nat. Methods* **10**, 1219–1224 (2013).
9. Filonov, G. S., Moon, J. D., Svensen, N. & Jaffrey, S. R. Broccoli: rapid selection of an RNA mimic of green fluorescent protein by fluorescence-based selection and directed evolution. *J. Am. Chem. Soc.* **136**, 16299–16308 (2014).
10. Dolgosheina, E. V. et al. RNA mango aptamer-fluorophore: a bright, high-affinity complex for RNA labeling and tracking. *ACS Chem. Biol.* **9**, 2412–2420 (2014).
11. Sunbul, M. & Jaschke, A. SRB-2: a promiscuous rainbow aptamer for live-cell RNA imaging. *Nucleic Acids Res.* **46**, e110 (2018).
12. Arora, A., Sunbul, M. & Jaschke, A. Dual-colour imaging of RNAs using quencher- and fluorophore-binding aptamers. *Nucleic Acids Res.* **43**, e144 (2015).
13. Sunbul, M. & Jaschke, A. Contact-mediated quenching for RNA imaging in bacteria with a fluorophore-binding aptamer. *Angew. Chem. Int. Ed. Engl.* **52**, 13401–13404 (2013).
14. Autour, A. et al. Fluorogenic RNA Mango aptamers for imaging small non-coding RNAs in mammalian cells. *Nat. Commun.* **9**, 656 (2018).
15. Li, X., Kim, H., Litke, J. L., Wu, J. & Jaffrey, S. R. Fluorophore-promoted RNA folding and photostability enables imaging of single Broccoli-tagged mRNAs in live mammalian cells. *Angew. Chem. Int. Ed. Engl.* **59**, 4511–4518 (2020).
16. Li, X. et al. Imaging intracellular S-adenosyl methionine dynamics in live mammalian cells with a genetically encoded red fluorescent RNA-based sensor. *J. Am. Chem. Soc.* **142**, 14117–14124 (2020).

17. Tan, X. et al. Fluoromodules consisting of a promiscuous RNA aptamer and red or blue fluorogenic cyanine dyes: selection, characterization, and bioimaging. *J. Am. Chem. Soc.* **139**, 9001–9009 (2017).

18. Braselmann, E. et al. A multicolor riboswitch-based platform for imaging of RNA in live mammalian cells. *Nat. Chem. Biol.* **14**, 964–971 (2018).

19. Bouhedda, F. et al. A dimerization-based fluorogenic dye-aptamer module for RNA imaging in live cells. *Nat. Chem. Biol.* **16**, 69–76 (2020).

20. Song, W. et al. Imaging RNA polymerase III transcription using a photostable RNA–fluorophore complex. *Nat. Chem. Biol.* **13**, 1187–1194 (2017).

21. Cawte, A. D., Unrau, P. J. & Rueda, D. S. Live cell imaging of single RNA molecules with fluorogenic Mango II arrays. *Nat. Commun.* **11**, 1283 (2020).

22. Sunbul, M. et al. Super-resolution RNA imaging using a rhodamine-binding aptamer with fast exchange kinetics. *Nat. Biotechnol.* **39**, 686–690 (2021).

23. Dey, S. K. et al. Publisher correction: Repurposing an adenine riboswitch into a fluorogenic imaging and sensing tag. *Nat. Chem. Biol.* **18**, 236 (2022).

24. Wirth, R., Gao, P., Nienhaus, G. U., Sunbul, M. & Jaschke, A. SiRA: a silicon rhodamine-binding aptamer for live-cell super-resolution RNA imaging. *J. Am. Chem. Soc.* **141**, 7562–7571 (2019).

25. Zhang, J., Wang, L., Jaschke, A. & Sunbul, M. A color-shifting near-infrared fluorescent aptamer-fluorophore module for live-cell RNA imaging. *Angew. Chem. Int. Ed. Engl.* **60**, 21441–21448 (2021).

26. Li, X., Wu, J. & Jaffrey, S. R. Engineering fluorophore recycling in a fluorogenic RNA aptamer. *Angew. Chem. Int. Ed. Engl.* **60**, 24153–24161 (2021).

27. Chen, X. et al. Visualizing RNA dynamics in live cells with bright and stable fluorescent RNAs. *Nat. Biotechnol.* **37**, 1287–1293 (2019).

28. Steinmetzger, C., Palanisamy, N., Gore, K. R. & Hobartner, C. A multicolor large Stokes shift fluorogen-activating RNA aptamer with cationic chromophores. *Chemistry* **25**, 1931–1935 (2019).

29. Huang, K. et al. Structure-based investigation of fluorogenic Pepper aptamer. *Nat. Chem. Biol.* **17**, 1289–1295 (2021).

30. Yuan, L., Lin, W. & Chen, H. Analogs of Changsha near-infrared dyes with large Stokes shifts for bioimaging. *Biomaterials* **34**, 9566–9571 (2013).

31. Grubbs, R. D. Intracellular magnesium and magnesium buffering. *Biometals* **15**, 251–259 (2002).

32. Prasanth, K. V. et al. Nuclear organization and dynamics of 7SK RNA in regulating gene expression. *Mol. Biol. Cell* **21**, 4184–4196 (2010).

33. Marnef, A., Richard, P., Pinzon, N. & Kiss, T. Targeting vertebrate intron-encoded box C/D 2'-O-methylation guide RNAs into the Cajal body. *Nucleic Acids Res.* **42**, 6616–6629 (2014).

34. Novotny, I. et al. SART3-dependent accumulation of incomplete spliceosomal snRNPs in Cajal bodies. *Cell Rep.* **10**, 429–440 (2015).

35. Tsalikis, J. et al. Intracellular bacterial pathogens trigger the formation of U small nuclear RNA bodies (U Bodies) through metabolic stress induction. *J. Biol. Chem.* **290**, 20904–20918 (2015).

36. Jain, S. et al. ATPase-modulated stress granules contain a diverse proteome and substructure. *Cell* **164**, 487–498 (2016).

37. Shao, S. et al. Long-term dual-color tracking of genomic loci by modified sgRNAs of the CRISPR/Cas9 system. *Nucleic Acids Res.* **44**, e86 (2016).

38. Chen, B. et al. Dynamic imaging of genomic loci in living human cells by an optimized CRISPR/Cas system. *Cell* **155**, 1479–1491 (2013).

39. Xiong, F. & Frasch, W. D. OmegaqPCR measures telomere length from single-cells in base pair units. *Nucleic Acids Res.* **49**, e120 (2021).

40. Hall, M. P. et al. Engineered luciferase reporter from a deep sea shrimp utilizing a novel imidazopyrazinone substrate. *ACS Chem. Biol.* **7**, 1848–1857 (2012).

41. Johansson, H. E. et al. A thermodynamic analysis of the sequence-specific binding of RNA by bacteriophage MS2 coat protein. *Proc. Natl Acad. Sci. USA* **95**, 9244–9249 (1998).

42. Grahn, E. et al. Structural basis of pyrimidine specificity in the MS2 RNA hairpin-coat-protein complex. *RNA* **7**, 1616–1627 (2001).

43. Franklin, N. C. 'N' transcription antitermination proteins of bacteriophages lambda, phi 21 and P22. *J. Mol. Biol.* **181**, 85–91 (1985).

44. Loughlin, F. E. et al. The zinc fingers of the SR-like protein ZRANB2 are single-stranded RNA-binding domains that recognize 5' splice site-like sequences. *Proc. Natl Acad. Sci. USA* **106**, 5581–5586 (2009).

45. Kondo, Y., Oubridge, C., van Roon, A. M. & Nagai, K. Crystal structure of human U1 snRNP, a small nuclear ribonucleoprotein particle, reveals the mechanism of 5' splice site recognition. *eLife* **4**, e04986 (2015).

46. Spritz, R. A., Strunk, K., Surowy, C. S. & Mohrenweiser, H. W. Human U1-70K ribonucleoprotein antigen gene: organization, nucleotide sequence, and mapping to locus 19q13.3. *Genomics* **8**, 371–379 (1990).

47. Wu, R. et al. Ratiometric fluorogenic RNA-based sensors for imaging live-cell dynamics of small molecules. *ACS Appl. Bio Mater.* **3**, 2633–2642 (2020).

48. Konig, K. Multiphoton microscopy in life sciences. *J. Microsc.* **200**, 83–104 (2000).

49. Protter, D. S. W. & Parker, R. Principles and properties of stress granules. *Trends Cell Biol.* **26**, 668–679 (2016).

## Methods

### SELEX

The SELEX experiment was performed according to previous studies[27]. In brief, a single-stranded DNA library containing two 26-base random stretches separated by a 12-base fixed sequence and flanked from the 5′ and 3′ ends with constant regions (Generay Biotech Shanghai) was used for polymerase chain reaction (PCR) amplification, and T7-RNA polymerase-based in vitro transcription was used for preparation of the RNA library for SELEX. The RNA library was first incubated for 30 min with 500 μl 'mock' resin. The flow-through RNAs from the mock resin were then incubated with 500 μl NBSI-conjugated resin for 30 min and washed with 1 ml selection buffer (40 mM HEPES, pH 7.4, 100 mM KCl, 5 mM MgCl₂, 5% dimethylsulfoxide) for the indicated times at each round: 6 times (rounds 1–3), 8 times (rounds 4–5), 10 times (round 6) and 12 times (rounds 7–8). The eluted RNAs from the last round were precipitated with 70% ethanol, reverse-transcribed and PCR amplified. The PCR products were ligated into pGEM-T Easy vector (Promega) and sequenced.

### In vitro characterization of Clivia

Unless otherwise stated, the in vitro characterization of Clivia was determined in buffer containing 40 mM HEPES, pH 7.4, 100 mM KCl and 5 mM MgCl₂. Absorption, excitation and emission spectra were measured according to previous studies[27]. In brief, excess RNA aptamer and limiting amount of fluorophore were used to ensure that no free fluorophore contributes to the absorbance or fluorescence signal. The RNA concentration was 20 μM for fluorescence measurements and 50 μM for absorption measurements, while the fluorophore concentrations were 2 μM and 5 μM, respectively. The extinction coefficient was calculated based on the absorption spectrum and the Beer–Lambert–Bouguer law. All quantum yields were determined by comparing the integral of the corrected emission spectra for each RNA–fluorophore complex with the corresponding integral obtained from a solution of rhodamine 6G (which was in water solution with a quantum yield of 0.95 when excited at 488 nm). All measurements for RNA–fluorophore complexes were taken in the presence of excess RNA to avoid interference from unbound fluorophore. To determine the dissociation constants of Clivia with different fluorophores, 20 nM Clivia RNA was incubated with increasing concentrations of the fluorophore (0–5 μM) and the fluorescence intensity at the corresponding spectra was measured using a Neo2 multi-mode microplate reader (BioTek). The resulting data were fitted to a curve based on the Hill equation: $Y = B_{max} \cdot X_h/(K_d + X_h)$, where $B_{max}$ represents the maximum specific binding parameter in the same units as Y, h represents the Hill slope and $K_d$ represents the concentration needed to achieve a half-maximum binding at equilibrium. To compare the magnesium dependence of Clivia with other fluorescent RNAs, 1 μM RNA aptamer (Clivia, Pepper or Corn) was incubated with 10 μM fluorophore (NBSI for Clivia, HBC599 for Pepper and DFHO for Corn) in 40 mM HEPES, pH 7.4, 100 mM KCl buffer containing different concentrations of MgCl₂ ranging from 0 mM to 5 mM. The fluorescence intensities at the indicated magnesium concentration were measured using a Neo2 multi-mode microplate reader (BioTek). To determine the thermostability of RNA–fluorophore complexes, 1 μM RNA was incubated with 10 μM fluorophore and the fluorescence intensities at the indicated temperatures (16–70 °C) were then recorded using a qTower cycler (Analytik Jena). To detect potassium dependence fluorescence for Clivia, 1 μM Clivia RNA was incubated with 5 μM NBSI in buffer containing 40 mM HEPES, 5 mM MgCl₂, with or without 100 mM KCl or LiCl. The RNA–fluorophore complex was heated to 70 °C for 5 min and cooled to room temperature over 15 min. Broccoli and Spinach 2, which contain a G-quadruplex structure, and Pepper, which does not contain a G-quadruplex structure, were used as the controls.

### DNA cloning

Complementary DNA encoding R8 embedded in a tRNA scaffold was synthesized by Beijing Liuhe BGI and inserted into pET28a-F30-D11

(ref. 27) to replace the F30-D11 fragment to obtain pET28a-tRNA-R8. For comparison of RNA imaging by Clivia with other fluorescent RNA tags, the cDNAs encoding tRNA-Clivia and tRNA-Chili were inserted into the original sgRNA expression plasmid using the pEASY-Basic Seamless Cloning and Assembly Kit (TransGen Biotech), which was linearized by PCR amplification to remove the native sgRNA scaffold[50]. All primers were synthesized by Nanjing Genscript Biotech. The obtained plasmids were named pU6-tRNA-Clivia and pU6-tRNA-Chili. For comparison of RNA imaging by different copies of Clivia, the cDNAs encoding different copies of Clivia arrays fused to a F30 scaffold were synthesized by Beijing Liuhe BGI and inserted into pU6-tRNA-Clivia to replace the tRNA-Clivia fragment. For imaging of diverse ncRNAs, the cDNAs of Clivia-U6, mgU2-Clivia and Clivia-7SK were synthesized and inserted into pU6-tRNA-Clivia to replace the tRNA-Clivia fragment. Reverse PCR was used to amply pU6-Clivia-U6 using primers containing cDNAs encoding different RNA tags. The linearized fragments were phosphatized and ligated to generate plasmids expressing different chimeric U6 snRNA. A similar strategy was used to generate plasmids expressing different chimeric U1 snRNA based on AT-U1 (Addgene: 112059). The Clivia fragments in the aforementioned plasmids were replaced with Chili fragments using reverse PCR to obtain plasmids expressing Chili-tagged snRNAs. For single-excitation two-emission dual-color imaging of two RNAs, primers containing sequences encoding Clivia-boxB and Pepper-MS2 were annealed and inserted into pU6-tRNA-Clivia to replace tRNA-Clivia using the pEASY-Basic Seamless Cloning and Assembly Kit. The SNAP tag gene fragment was amplified from pcDNA3.1-SNAP-4Pepper[27] and inserted into pH2B-tdMCP-BFP[27] to replace BFP to obtain pH2B-tdMCP-SNAP. cDNA encoding the N peptide was synthesized, amplified and inserted into the 5′ end of TOMM20 in pcDNA3.1-TOMM20-tdMCP-BFP[27]. The obtained plasmid was amplified using reverse PCR to remove the tdMCP fragment to generate pcDNA3.1-N-TOMM20-BFP. For single-molecule RNA imaging, DNA fragments encoding 8Clivia and 8xMS2 were synthesized and inserted into the 3′ untranslated region of the ACTB gene in pcDNA3.1-ACTB-4Pepper[27] to generate pcDNA3.1-ACTB-8Clivia-8xMS2. The obtained plasmid was amplified using reverse PCR to introduce a 2xPP7 fragment to generate pcDNA3.1-ACTB-8Clivia-8xMS2-2xPP7. Gene fragment encoding tdPCP protein was amplified from pHAGE-Ubc-NLS-HA-tdPCP-GFP (Addgene: 40650) and inserted into pCMV-LicV-mKalama1-CAAX[50] to obtain pCMV-tdPCP-CAAX. For single-excitation two-emission dual-color imaging of multiple genomic loci, sgRNA-4R8 was synthesized and inserted into pSgRNA-Pepper[27] to generate pSgRNA-4R8. Primers containing different genomic loci targeting sequences were used to amplify pSgRNA-4R8 and pSgRNA-4Pepper. The linearized fragments were phosphatized and ligated to generate plasmids expressing chimeric sgRNAs targeting different genomic loci (Supplementary Table 2). For detection of RNA–protein interaction in live cells, an NLuc gene fragment was inserted into multiple cloning sites of pcDNA3.1 hygro (+) to generate pcDNA3.1-NLuc. The MCP gene fragment was inserted into the 3′ end of NLuc in pcDNA3.1-NLuc to generate pcDNA3.1-NLuc-MCP. Gene fragment encoding cpMCP was obtained by fusing 1–66 amino acids of NLuc to the carboxy terminal of NLuc with an LESR amino acid linker. Then the cpMCP fragment was inserted into pcDNA3.1-NLuc-MCP to replace MCP to generate pcDNA3.1-NLuc-cpMCP. Another MCP gene fragment was inserted into the LESR linker region of cpMCP in pcDNA3.1-NLuc-cpMCP to generate pcDNA3.1-NLuc-dMCP. Reverse PCR was used to amplify pcDNA3.1-NLuc-dMCP to generate plasmids expressing NLuc-dMCP mutants containing different dMCP variants and linkers between NLuc and dMCP. λ_N gene fragment was inserted into the 3′ end of NLuc in pcDNA3.1-NLuc to generate pcDNA3.1-NLuc-λ_N. cDNAs encoding different RNA binding proteins were amplified from the Human ORFeome Library (Thermo) and inserted into pcDNA3.1-NLuc to generate plasmids expressing different BRET fusion proteins. cDNAs encoding ribozyme-flanked[51] Clivia-MS2

and Clivia-MS2 (5′), and Clivia-MS2 (3′) and Clivia-boxB were synthesized and inserted into pU6-tRNA-Clivia to generate pU6-Cir-Clivia-MS2 and pU6-Cir-Clivia-boxB, respectively, using the pEASY-Basic Seamless Cloning and Assembly Kit. The MS2 hairpin was replaced by other RNA sequences using reverse PCR to generate RNA reporter plasmids for detection of other RNA–protein interactions. DNA fragment encoding 7SL lncRNA was synthesized and inserted into pU6-Cir-Clivia-MS2 to generate pU6-7SL. The obtained plasmid was amplified using reverse PCR to generate pU6-7SL-Clivia-MS2. The AT-U1 (Addgene: 112059) plasmid was amplified to remove the AT sequence to obtain plasmid expressing U1 alone. The obtained plasmid was amplified using primers containing a Clivia-encoding sequence by inserting Clivia into different stem-loops of U1 snRNA. DNA fragment encoding the 1–194 amino acids of U1-70K was synthesized, amplified and inserted into pcDNA3.1-NLuc to generate pcDNA3.1-U1-70K$_{(1-194)}$-NLuc. The sequence information is given in Supplementary Note 2.

## Cell culture and transfection

HEK293T (GNHu44) and HeLa (TCHu187) were purchased from the Cell Bank of the Chinese Academy. HeLa cells were cultured in high-glucose DMEM supplemented with 10% fetal bovine serum (FBS). HEK293T cells were maintained in RPMI 1640 with 10% FBS. The cell lines were authenticated and mycoplasma negative. The cells were cultured at 37 °C in a humidified atmosphere of 95% air and 5% $CO_2$ and split every 2 days. Unless otherwise indicated, transfection of HEK293T and HeLa cells were performed using Hieff Trans Liposomal Transfection Reagent (Yeasen) according to the manufacturer's recommendations: 0.4 µg DNA and 1.2 µl transfection reagent were mixed with 50 µl Opti-MEM and incubated for 20 min at room temperature. The mixture was added to each chamber of 35 mm four-chamber glass bottom dishes with number 1 cover glass (Cellvis) with cells at 40–60% confluence.

## Cytotoxicity assays

HeLa cells were grown in Corning 96-well plates at a confluency of 5,000 cells per well in 65 µl of fresh medium. After 24 h, cells were incubated with 65 µl medium plus 0–5 µM fluorophores and incubated for another 48 h. Control cells were incubated with 65 µl medium in the absence of any fluorophore. Cells were then washed several times with PBS and assayed for cell viability with the CCK-8 Kit (Cell Counting Kit from Yeasen) according to the manufacturer's instructions. Absorbance at 450 nm was determined using a Neo2 microplate reader (BioTek).

## Imaging

Unless otherwise specified, the transfected mammalian cells were incubated with the corresponding fluorophores in DMEM with 10% FBS without phenol red for 10 min at 37 °C in a humidified atmosphere of 95% air and 5% $CO_2$ before imaging.

**RNA imaging by NBSI and its analogs.** For comparison of Clivia and Chili fluorescent RNA, plasmids expressing tRNA-Clivia or tRNA-Chili were transfected into HEK293T cells. The cells were incubated with 1 µg ml$^{-1}$ Hoechst 33342 and 0.2 µM NBSI, 1 µM DMHBI-lmi or 1 µM DMHBO$^+$ (synthesized by Shanghai Haohong Scientific), respectively. For comparison of different copies of Clivia arrays, plasmids expressing different copies of Clivia arrays were transfected into HEK293T cells. The cells were incubated with 1 µg ml$^{-1}$ Hoechst 33342 and 0.2 µM NBSI. Fluorescence imaging was performed using a Leica SP8 confocal laser scanning microscope equipped with an HC PL APO CS2 ×63.0/numerical aperture (NA) 1.40 oil objective and a HyD detector, using 405 nm laser excitation for Hoechst 33342 and TagBFP, and a 497 nm laser for Clivia-NBSI, Chili-DMHBI-lmi and Chili-DMHBO$^+$. To detect RNA imaging by NBSI analogs, plasmid expressing 4Clivia was transfected into HEK293T cells. The cells were incubated with 0.2 or 0.5 µM NBSI analogs and 1 µg ml$^{-1}$ Hoechst 33342. Fluorescence imaging was performed using a Leica SP8 confocal laser scanning

microscope equipped with an HC PL APO CS2 ×63.0/NA 1.40 oil objective and a HyD detector, using 405 nm laser excitation for Hoechst 33342 and TagBFP, 514 nm laser single-photon excitation for NBSI565, NBSI570, NBSI571, NBSI574, NBSI578, NBSI595 and NBSI618, 561 nm laser single-photon excitation for NBSI577, NBSI581, NBSI582, NBSI590, NBSI600 and NBSI624, and 1,040 nm two-photon excitation for all Clivias. The image processing was performed using the Leica Application Suite X or ImageJ software.

To determine photostability of fluorescent RNAs and fluorescent proteins in living cells, a continuous 488 nm laser single-photon excitation (20 µW, ×60 objective) or a continuous 976 nm laser two-photon excitation (27 mW, ×63 objective) was used for different Clivias, Chili-DMHBI-lmi and CyOFP1. The output powers of the laser lines were measured using a Laser Power Meter LP1 (Sanwa).

**Imaging of small nuclear RNAs.** To image snRNA labeling by Clivia and Chili, plasmid expressing Clivia-U6 or Chili-U6 was co-transfected with pCDNA3.1-SART3-BFP (6:4; a total of 0.5 µg plasmids for a 35 mm four-chamber glass bottom dish) into HEK293T cells; plasmid expressing Clivia-U1 and Chili-U1 was transfected into HEK293T cells; plasmid expressing Clivia-7SK or Chili-7SK was co-transfected with pCDNA3.1-SC35-BFP (6:4; a total of 0.5 µg plasmids for a 35 mm four-chamber glass bottom dish) into HEK293T cells; plasmid expressing Clivia-mgU2-47 or Chili-mgU2-47 was co-transfected with pCDNA3.1-Coilin-GFP (6:4; a total of 0.5 µg plasmids for a 35 mm four-chamber glass bottom dish) into HEK293T cells. The cells were incubated with 1 µM NBSI618 (Clivia-U6 and Clivia-U1) or 1 µM DMHBI-lmi (Chili-U6 and Chili-U1) 36 h after transfection. For U1 snRNA imaging, HEK293T cells transfected with plasmids encoding Clivia-U1 or SMN1-GFP and different chimeric Clivia-U1 reporters (1:9) were treated with 10 µM thapsigargin for 3 h and the nuclei were stained with 1 µg ml$^{-1}$ Hoechst 33342 before imaging. The cells were imaged using a Leica SP8 confocal laser scanning microscope or an inverted Nikon (TI-E) microscope equipped with a Nikon Perfect Focus system, a PL APO VC ×100/NA 1.40 oil objective or an APO ×60/NA 1.40 oil objective and a photometrics Prime 95B sCMOS camera, with 405 nm laser excitation for Hoechst 33342 and TagBFP, 488 nm laser excitation for Chili-DMHBI-lmi and 561 nm laser excitation for NBSI618. For imaging of U1 snRNA dynamics, Z-stack images were taken with a step size of 1 µm and enough steps to cover the depth of each cell. Maximum intensity projection of the z-stack images was processed using the NIS-Elements AR software.

For super-resolution imaging of small snRNAs, SIM was performed using a Nikon N-SIM S super-resolution imaging microscope. Fluorescence was excited using a 561 nm laser and a 590–650 nm filter for Clivia624, and a 405 nm laser and 435–485 nm filter for tagBFP with five rotations of the grid pattern, and images were collected using a Nikon SR HP Apo TIRF ×100/NA 1.49 oil objective. Acquisition was performed using a complementary metal-oxide semiconductor with a frame size of 1,024 × 1,024 pixels. Three reconstruction parameters (illumination modulation contrast, high-resolution noise suppression and out of focus blur suppression) were extensively tested to generate consistent images across experiments without abnormal features or artifacts and with the best Fourier transforms. All SIM image processing was performed using the NIS-Elements AR software.

**Single-molecule RNA imaging.** To perform single-molecule RNA imaging, HeLa cells were transfected with ACTB-8Clivia-8xMS2-2xPP7, NLS-tdMCP-GFP and tdPCP-CAAX (5:1:4; a total of 0.5 µg plasmids for a 35 mm four-chamber glass bottom dish). At 24 h after transfection, the cells were incubated with 50 nM NBSI624 and imaged with an inverted Nikon (TI-E) microscope equipped with a Nikon Perfect Focus system, a PL APO VC ×100/NA 1.40 oil objective and a photometrics Prime 95B sCMOS camera, with 488 nm laser excitation for GFP and 561 nm laser excitation for Clivia624.

**Single-excitation two-emission fluorescence imaging of RNA and genomic loci.** To image protein-tethered RNA, plasmids expressing Pepper-boxB, Clivia-MS2, tdMCP-SNAP-H2B and N-TOMM20-BFP were co-transfected (6:6:4:4; a total of 0.5 μg plasmids for a 35 mm four-chamber glass bottom dish) into HEK293T cells. The cells were incubated with 0.5 μM NBSI analogs, 1 μM HBC497 or HBC analogs (FR Biotechnology) and 0.2 μM SNAP-Cell 647-SiR (NEB) 36 h after transfection. Fluorescence imaging was performed using a Leica SP8 confocal laser scanning microscope equipped with an HC PL APO CS2 ×63.0/NA 1.40 oil objective and a HyD detector using 405 nm laser excitation for TagBFP, 488 nm laser excitation for Clivias, Pepper497 and Pepper530, emission at 495–530 nm for Pepper530, emission at 630–680 nm for Clivia618, emission at 495–520 nm for Pepper497 and emission at 610–650 nm for other Clivias, and 633 nm laser excitation and emission at 640–740 nm for SNAP-SiR. For simultaneous imaging of ACTB and U6, plasmids expressing ACTB-4Pepper, Clivia-U6 and SART3-BFP were co-transfected (1:1:1; a total of 0.5 μg plasmids for a 35 mm four-chamber glass bottom dish) into HEK293T cells. The cells were incubated with 0.5 μM NBSI595 and 1 μM HBC497 24 h after transfection. Single-photon (a 488 nm laser) or two-photon (a 976 nm laser) imaging for living cells was performed using a Leica SP8 confocal laser scanning microscope or Leica TCS SP8 DIVE microscope equipped with an HC PL APO CS2 ×63.0/NA 1.40 oil objective and HyD detector, with emission at 495–520 nm for Pepper497 and emission at 610–650 nm for NBSI595.

To image genomic loci with Clivia and Pepper, pSgRNA-4Clivia (cent) and pCDNA3-dCas9-SNAP, pSgRNA-4Pepper (telo) and pCDNA3-dCas9-SNAP were co-transfected (1:1; a total of 0.5 μg plasmids for a 35 mm four-chamber glass bottom dish) into HEK293T cells. The cells were incubated with 0.2 μM SNAP-Cell 647-SiR (NEB), 1 μg ml⁻¹ Hoechst 33342 and 0.2 μM NBSI or 1 μM HBC497 36 h after transfection. pSgRNA-4Clivia (cent) and pSgRNA-4Pepper (telo), pSgRNA-4Clivia (C9-1) and pSgRNA-4Pepper (C9-2), pSgRNA-4Clivia (C13-1) and pSgRNA-4Pepper (C13-2), pSgRNA-4Clivia (C19-2) and pSgRNA-4Pepper (C19-1) were co-transfected with pCDNA3-dCas9-SNAP (3:3:4 a total of 0.5 μg plasmids for a 35 mm four-chamber glass bottom dish) into HEK293T cells; pSgRNA-4Clivia (C9-2), pSgRNA-4Clivia (C19-1), pSgRNA-4Pepper(C13-1) and pSgRNA-4Pepper (C19-1) were co-transfected with pCDNA3-dCas9-SNAP (3:3:4; a total of 0.5 μg plasmids for a 35 mm four-chamber glass bottom dish) into HEK293T cells. The cells were incubated with 0.5 μM NBSI595, 1 μM HBC497 and 1 μg ml⁻¹ Hoechst 33342 36 h after transfection. Z-stack images were taken with a step size of 1 μm and enough steps to cover the depth of each nucleus using an inverted Nikon (TI-E) microscope equipped with a Nikon Perfect Focus system, a PL APO VC ×100/NA 1.40 oil objective and a photometrics Prime 95B sCMOS camera, with 405 nm laser excitation and emission at 435–485 nm for TagBFP and Hoechst 33342, 488 nm laser excitation and emission at 515–555 nm for Pepper497, 488 nm laser excitation and emission at 590–650 nm for Clivia595, and 640 nm laser excitation for SNAP-SiR. Maximum intensity projection of the z-stack images was processed using the NIS-Elements AR software.

To derive the approximate telomere length, HEK293T cells were co-transfected with plasmids expressing dCas9-SNAP and Pepper-tagged sgRNA targeting the genomic locus with varied copy number (1:1). The cells were incubated with 0.2 μM SNAP-Cell 647-SiR (NEB), 1 μg ml⁻¹ Hoechst 33342 and 1 μM HBC497 36 h after transfection. Fluorescence imaging was performed using an inverted Nikon (TI-E) microscope equipped with a Nikon Perfect Focus system, a PL APO VC ×100/NA 1.40 oil objective and a photometrics Prime 95B sCMOS camera, with 405 nm laser excitation for Hoechst 33342, 488 nm laser excitation for Pepper497 and 640 nm laser excitation for SNAP-SiR. The fluorescence intensities of the foci were quantified using the ImageJ software. The data were fitted to a linear equation and were then used as the standard curve for measuring the copy number of telomeres from their fluorescent signals.

**Bioluminescence imaging of RNA–protein interaction.** Plasmids expressing NLuc fusion protein and Clivia chimeric RNA were co-transfected (1:20; a total of 0.1 μg plasmids per well of a glass bottom 96-well plate) into HEK293T cells. To compare the BRET signals in the cells during the interphase and mitotic phase, plasmids expressing Clivia-U1-SL3, U1-70K$_{(1–194)}$-NLuc and LaminA-SNAP (17:2:1; a total of 0.1 μg plasmids per well of a glass bottom 96-well plate) were co-transfected into HEK293T cells. The cells were incubated with 1 μM NBSI574 or other NBSI analogs or 1 μM NBSI574 and 0.2 μM SNAP-Cell 647-SiR for 10 min, 24 h after transfection. To compare the BRET signals in the nucleoplasm and in U-bodies, the cells were treated with 10 μM thapsigargin for 3 h before imaging. The bioluminescence spectrum was measured immediately after the addition of furimazine (final concentration was 10 μM) using a Neo2 multi-mode microplate reader (BioTek). Bioluminescence imaging was performed using a Nikon eclipse Ti2 microscope equipped with CSU-W1, a PL APO VC ×60/NA 1.40 oil objective and a photometrics Prime 95B sCMOS camera, with a 460 ± 25 nm filter for NLuc emission and a 620 ± 30 nm filter for Clivia emission.

For in vivo luminescence imaging, all procedures involving animals were approved by the Institutional Animal Care and Use Committee of East China University of Science and Technology. Any experiments involving live animals must conform to relevant national and institutional regulations. Four-week-old male KM mice (Shanghai Jie Si Jie Laboratory Animal Co. Ltd) were used for the animal experiments. The mice were kept at 18–23 °C with 40–60% humidity under a 12 h light–12 h dark cycle. A total of $1 \times 10^6$ engineered cells expressing NLuc fusion protein and Clivia chimeric RNA were incubated with 1 μM NBSI581 for 30 min and were implanted into the dorsal subcutaneous area of the mice. Bioluminescence imaging was performed using an IVIS Spectrum CT from PerkinElmer with a 500/20 nm bandpass filter for emission and a 600/20 nm bandpass filter for Clivia emission after in situ injection of 50 μl 20 μM furimazine. BRET efficiency was defined as the ratio of light intensity of 600/20 nm emission to that of 500/20 nm emission.

## Fluorescence detection in *Escherichia coli*

*E. coli* strain *BL21 Star (DE3)* was used for analysis of the fluorescence of R8 aptamer. The *E. coli* cells were transformed with pET28a-tRNA-R8 or empty pET28a plasmid and grown in Luria–Bertani medium supplemented with 50 μg ml⁻¹ kanamycin at 37 °C. Aptamer expression was induced by addition of 1 mM IPTG at an optical density at 600 nm of around 0.4. Four hours after induction, the cells were collected and incubated with buffer containing 40 mM HEPES, pH 7.4, 125 mM KCl, 5 mM MgCl$_2$ and 0.5 μM NBSI. The fluorescence was analyzed using a CytoFLEX-S flow cytometer (Beckman Coulter) with an excitation of 561/10 nm and an emission of 610/20 nm. The gate was placed based on the BL21 Star (DE3) cells transformed with empty vector and incubated with 0.5 μM NBSI to determine the population fraction that expressed tRNA-R8. The data processing was performed using the Cytexpert program.

## Fluorescence in situ hybridization and immunofluorescence

HEK293T cells were seeded on fibronectin-coated four-well dishes. Twenty-four hours after transfection, Clivia618 fluorescence was imaged upon incubation with 0.5 μM NBSI618, and the position coordinates of the cells were recorded using a Leica SP8 confocal laser scanning microscope or a Nikon (TI-E) spinning disk confocal microscope. The cells were then fixed with 4% paraformaldehyde in PBS and followed by three washes with PBS. The cells were permeabilized with 0.5% Triton X-100, 2 mM ribonucleoside vanadyl complexes and then left to stand in 70% ethanol at 4 °C overnight. After washing twice with 50% formamide and 2× SSC, hybridization was performed with 200 ng Cy3-labeled DNA probe in hybridization solution (50% formamide, 2× SSC, 2 mg ml⁻¹ yeast tRNA, 10% dextran sulfate) overnight at 37 °C.

The Cy3-probes were prepared using the Nick Translation Mix (Roche) (supplemented with Cy3-dUTP (Enzolife)) with the primers in Supplementary Table 3, and purified using an ethanol precipitation method. After washing with 50% formamide, 2× SSC at 37 °C for 2 × 10 min, the cells were blocked using 1% BSA, 1 mg ml⁻¹ yeast tRNA, 2 mM ribonucleoside vanadyl complexes, 8% formamide for 30 min and then incubated with Anti-SMN1/Gemin 1 antibody (Abcam, Mouse, 1:200) for 1 h at room temperature. The cells were then washed with 2× SSC for 3 × 5 min and incubated with Anti-Mouse IgG H&L (Alexa Fluor 488) (Abcam, Goat, 1:200) for 1 h at room temperature. The cells were then washed with 2× SSC for 3 ×5 min and followed by counterstain of the DNA using DAPI. The staining was imaged by adjusting the fixed cells to the recorded position coordinates. Imaging was performed using a Leica SP8 confocal laser scanning microscope or a Yokogawa CSU-W1 SoRa spinning disk confocal attached to an inverted Nikon (TI-E) microscope with the Nikon Perfect Focus system, a Plan Apo VC ×100/NA 1.40 oil objective, a photometrics Prime 95B sCMOS camera, using 405 nm laser excitation for DAPI and TagBFP, 488 nm laser excitation for Alexa Fluor 488 and 561 nm laser excitation for Clivia618 and Rhodamine.

### Fluorophore synthesis

Detailed information on fluorophore synthesis is given in Supplementary Notes 3 and 4.

### Statistical analysis

For experiments with duplicates, the results are shown as mean ± s.d., unless stated otherwise. GraphPad Prism and SigmaPlot were used for plotting, data fitting, graphing and statistical analysis. For comparison of the RNA imaging in the presence and absence of extra $Mg^{2+}$ in the image buffer, comparison of fluorescence contrast of U6 labeling by different RNA tags, comparison of BRET efficiency of MS2-MCP and boxB-$\lambda_N$ with the control cells or mice, comparison of BRET efficiencies of different ssRNA variants, different U1-Clivia chimeric RNAs and different U1-70K-NLuc fusion proteins, as well as comparison of BRET efficiencies between U1-70K$_{(1–194)}$-NLuc and U1-Clivia-SL3 in the U-bodies and in nucleoplasm or in non-mitotic and mitotic cells, analysis was performed using the two-tailed Student's $t$-test (Figs. 1g and 5h,k,n, Supplementary Figs. 6, 9f, 10b,d,12e and 13b,d,f,h,j,l,n, and Extended Data Figs. 9d and 10c,f,h), and all the $P$ values are listed in Supplementary Table 4.

### Reporting summary

Further information on research design is available in the Nature Portfolio Reporting Summary linked to this article.

## Data availability

The data supporting the findings of this study are available in the paper and its Supplementary Information files. Source data are provided with this paper.

## References

50. Liu, R. et al. Optogenetic control of RNA function and metabolism using engineered light-switchable RNA-binding proteins. *Nat. Biotechnol.* **40**, 779–786 (2022).

51. Litke, J. L. & Jaffrey, S. R. Highly efficient expression of circular RNA aptamers in cells using autocatalytic transcripts. *Nat. Biotechnol.* **37**, 667–675 (2019).

## Additional information

**Extended data** is available for this paper at https://doi.org/10.1038/s41592-023-01997-7.

**Supplementary information** The online version contains supplementary material available at https://doi.org/10.1038/s41592-023-01997-7.

**Correspondence and requests for materials** should be addressed to Xianjun Chen, Aiming Ren, Linyong Zhu or Yi Yang.

**Peer review information** *Nature Methods* thanks Gal Haimovich and the other, anonymous, reviewer(s) for their contribution to the peer review of this work. Primary Handling Editor: Rita Strack, in collaboration with the *Nature Methods* team.

**Reprints and permissions information** is available at www.nature.com/reprints.
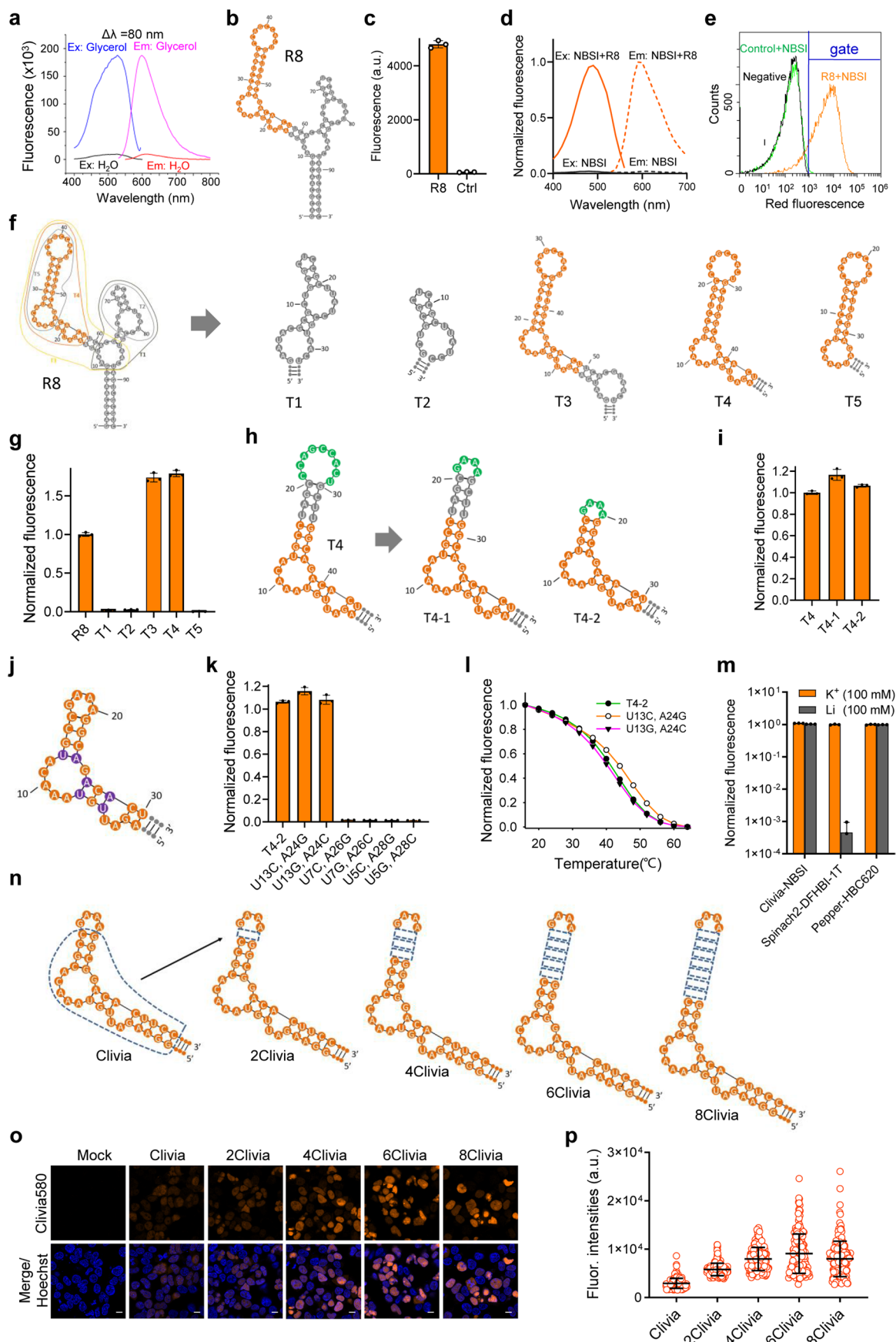
**Extended Data Fig. 1 | See next page for caption.**

**Extended Data Fig. 1 | Screening, optimization and characterization of Clivia.**
(a) Excitation and emission spectra of NBSI in glycerol. NBSI showed minimal fluorescence in water, but emitted bright fluorescence in glycerol. Δλ represents the Stokes shift. (b) The Mfold-predicted secondary structure of R8 aptamer. (c) Fluorescence activation of NBSI by R8 aptamer. (d) The excitation and emission spectra of R8-NBSI complex and NBSI alone. (e) FACS analysis of R8-NBSI complexes in BL21 Star™ (DE3) cells. *E. coli*. BL21 Star™ (DE3) cells expressing tRNA-R8 were induced by adding IPTG at 37 °C for 4 h. The cells were collected and incubated with 0.5 μM NBSI in HEPES buffer (containing 5 mM $Mg^{2+}$). Fluorescence was analyzed using a flow cytometry with a 561 nm excitation. The gate (blue) was placed based on the BL21 Star™ (DE3) cells transformed with empty vector and incubated with 0.5 μM NBSI to determine population fraction that expressed tRNA-R8. (f) The Mfold-predicted secondary structures of R8 and its truncation mutants. (g) Quantification of NBSI fluorescence induced by R8 and its truncation mutants. The markedly reduced fluorescence of the T5 aptamer suggests that T4 is the minimal aptamer sequence required for activation of NBSI fluorescence. (h) Stem-loop indicated in R8-T4 structure was replaced by other stem-loops with difference sequences. (i) Quantification of fluorescence of R8-T4 with different stem-loops. (j) Mutation sites (purple nucleotides) in T4-2. (k) Quantification of fluorescence of T4-2 mutants. (l) Thermostability of different T4-2 mutants. (m) Potassium independence for Clivia-induced fluorescence. (n) Schematic representation of different tandem arrays of Clivia. (o) Live cell imaging of different tandem arrays of Clivia in HEK293T cells. The cells were incubated with 0.2 μM NBSI for 10 min before imaging. Scale bar, 10 μm. (p) Quantification analysis of the fluorescence for different Clivia arrays in live cells. Data represent the mean ± s.d. (n = 200 cells). Data in (c), (g), (i), (k), (l), (m) represent the mean ± s.d. from three biologically independent replicates.
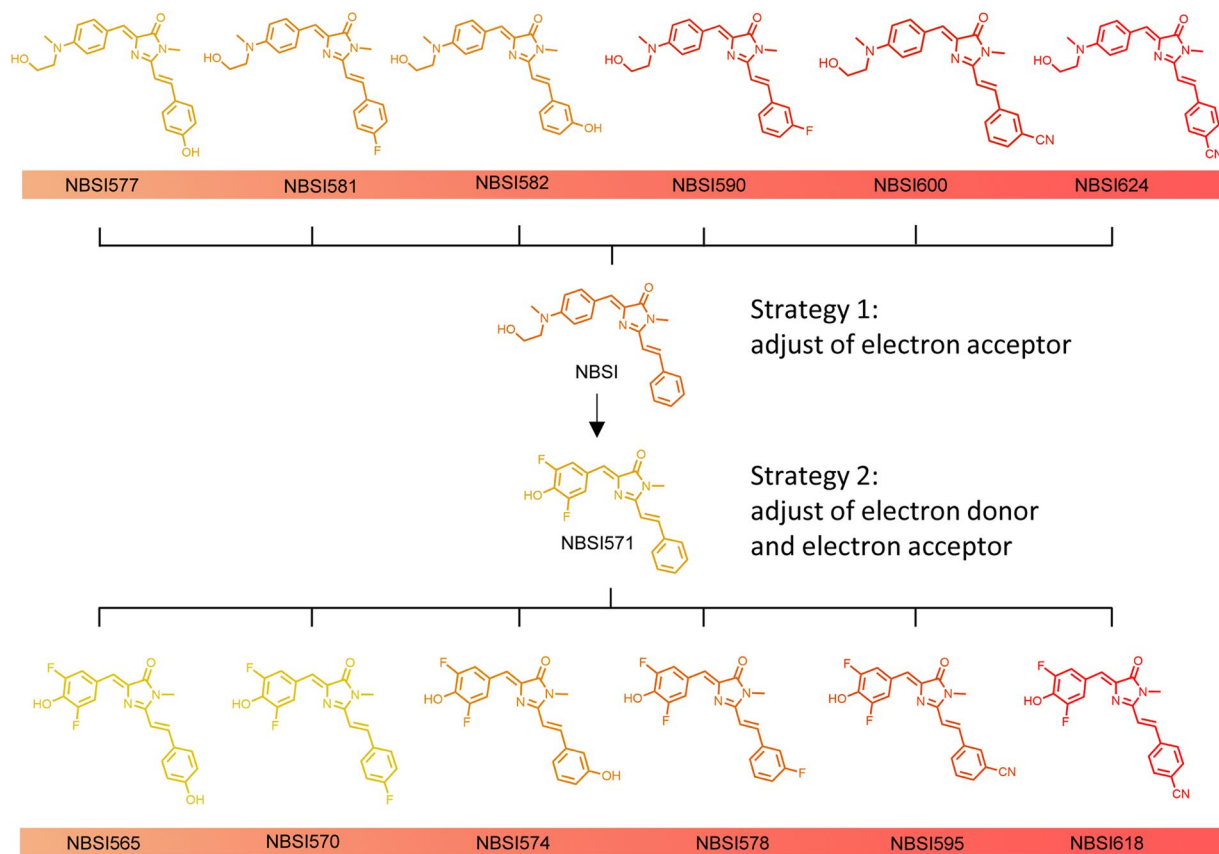
**Extended Data Fig. 2 | Strategy to tune the spectra of fluorophores.** NBSI has a typical dye molecular structure, including electron donor, electron acceptor and π conjugate structure. Thus, it is possible to fine tune the photophysical properties of NBSI by adjusting the length of π conjugate structure, the electron withdrawing capability of the electron acceptor group or the electron donating capability of the electron donor group. To keep the large Stokes shifts of the fluorophores, two strategies were conducted to fine tune the spectra characteristics of the fluorophores: Strategy 1: substitute the electron acceptor group by introducing different substituents on the benzene to adjust the electron withdrawing ability of NBSI. Strategy 2: substitute the electron donor group with phenol hydroxyl group and meanwhile introduce two fluorine atoms at its adjacent positions. Then, substitute the electron acceptor group described in strategy 1.
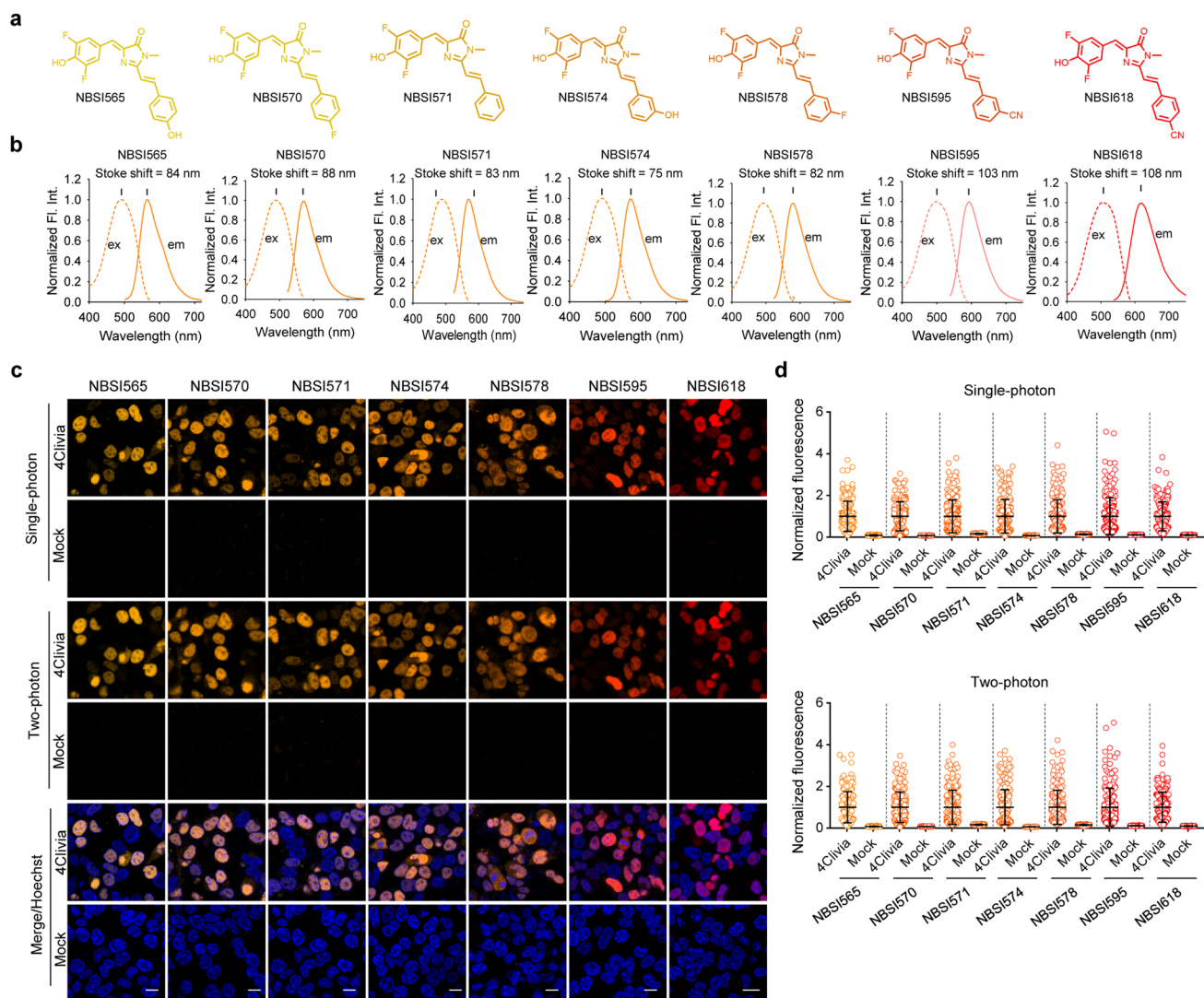
**Extended Data Fig. 3 | A palette of Clivias FRs with large Stokes shifts.**
**(a)** Structures of NBSI-like fluorophores. **(b)** Excitation (dashed) and emission (solid) spectra of the Clivias and their Stokes shifts were indicated. **(c)** Imaging of HEK293T cells expressing 4Clivia and incubated with 0.5 µM various NBSI-like fluorophores. Cells transfected with the empty vector were used as controls.

The nucleus was stained with 1 µg/ml Hoechst 33342 (blue). Scale bars, 10 µm.
**(d)** Quantification analysis of the fluorescence for different RNA–fluorophore complexes in live cells. The data were normalized to the average fluorescence of each RNA–fluorophore complex, respectively. Data represent the mean ± s.d. (n = 200 cells).
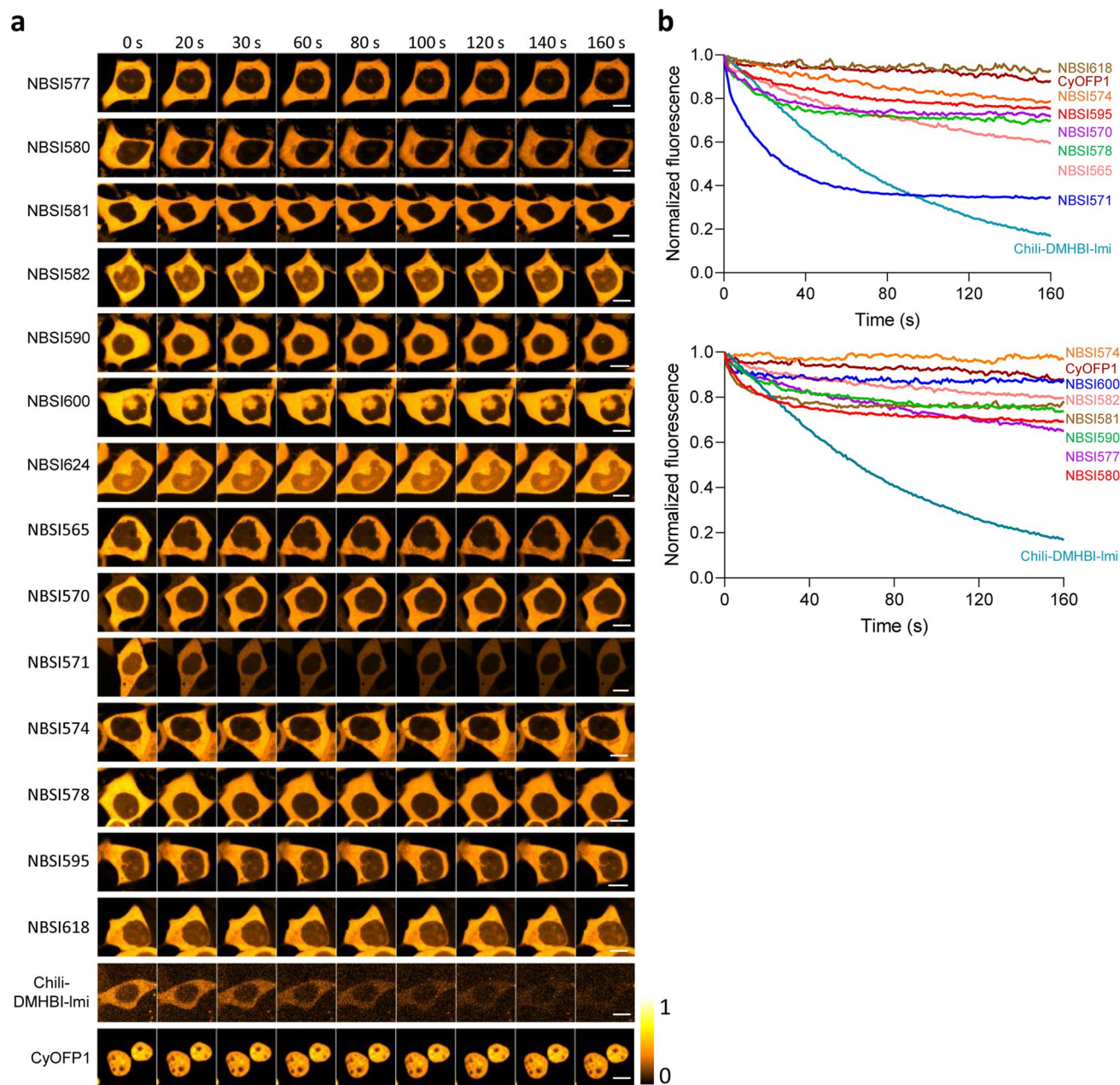
**Extended Data Fig. 4 | Photostability of different FRs and FP in single-photon excitation. (a)** HEK293T cells expressing tRNA-Clivia or tRNA-Chili were labeled with 0.5 µM NBSI and its analogs or 1 µM DMHBI-lmi. Continuous fluorescence imaging was performed using a spinning disk confocal laser scanning microscope with a 488 nm single-photon excitation. Cells expressing CyOFP1-H2B were used as the controls. Scale bars, 10 µm. **(b)** Quantification of the fluorescence in **(a)**. Data were normalized to the initial image intensity (at time 0), N=10 cells.
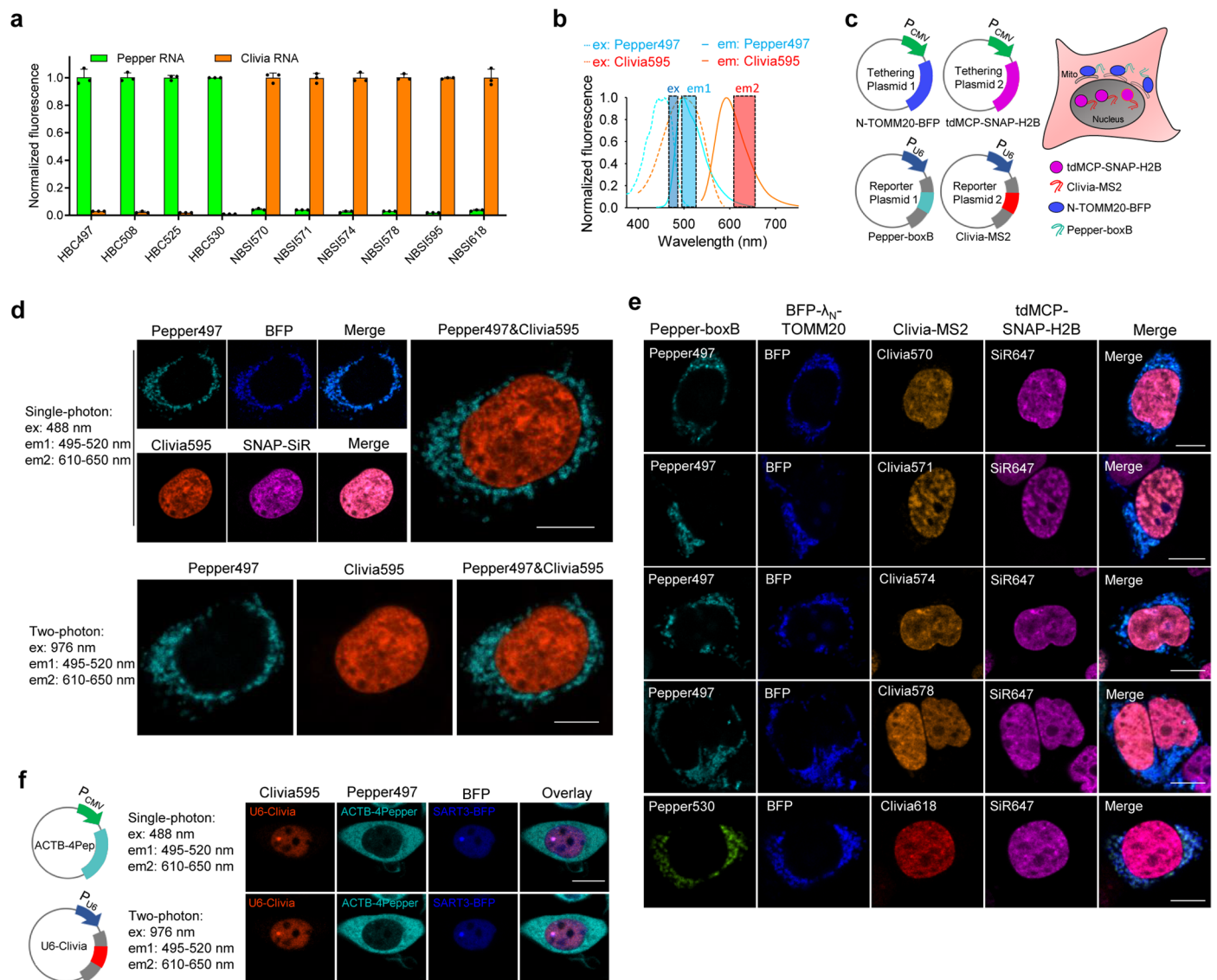
**Extended Data Fig. 5 | Dual-color imaging of two RNAs using Clivia and Pepper. (a)** The bio-orthogonality of Clivias with Peppers. Activation of HBC or NBSI ligands by Pepper or Clivia using 1 μM ligands and 5 μM aptamer. Data represent the mean ± s.d. from three biologically independent replicates. **(b)** The excitation and emission spectra of Clivia595 and Pepper497. **(c)** Schematic representation of the protein–RNA tethered reporting system based on the interaction of MCP and the MS2 binding hairpin RNA, as well as $\lambda_N$ and the boxB-binding hairpin RNA. **(d)** Imaging of HEK293T cells expressing Clivia-MS2, tdMCP-SNAP-H2B, Pepper-boxB and N-TOMM20-BFP that targeted the nucleus and outer mitochondrial membrane, respectively, using a single excitation in single-photon and two-photon microcopy. The cells were labeled with 0.5 μM

NBSI595, 1 μM HBC497 and 0.2 μM SNAP-Cell 647-SiR. Scale bar, 10 μm. **(e)** Single-excitation two-emission dual-color imaging of two tethered RNAs using different Clivia and Pepper combinations. HEK293T cells were transfected with plasmids expressing Clivia-MS2, MCP-SNAP-H2B, Pepper-boxB and $\lambda_N$-TOMM20-BFP that targeted to nucleus and outer mitochondrial membrane, respectively. Thirty-six hrs after transfection, the cells were incubated with HBC497 and NBSI570, HBC497 and NBSI571, HBC497 and NBSI574, HBC497 and NBSI578 or HBC530 and NBSI618. Scale bars, 10 μm. **(f)** Single-excitation two-emission dual-color imaging of U6 snRNA and ACTB mRNA using Clivia and Pepper in single-photon or two-photon microcopy, respectively. Scale bars, 10 μm.

**a**



Thapsigargin

**b**



**c**
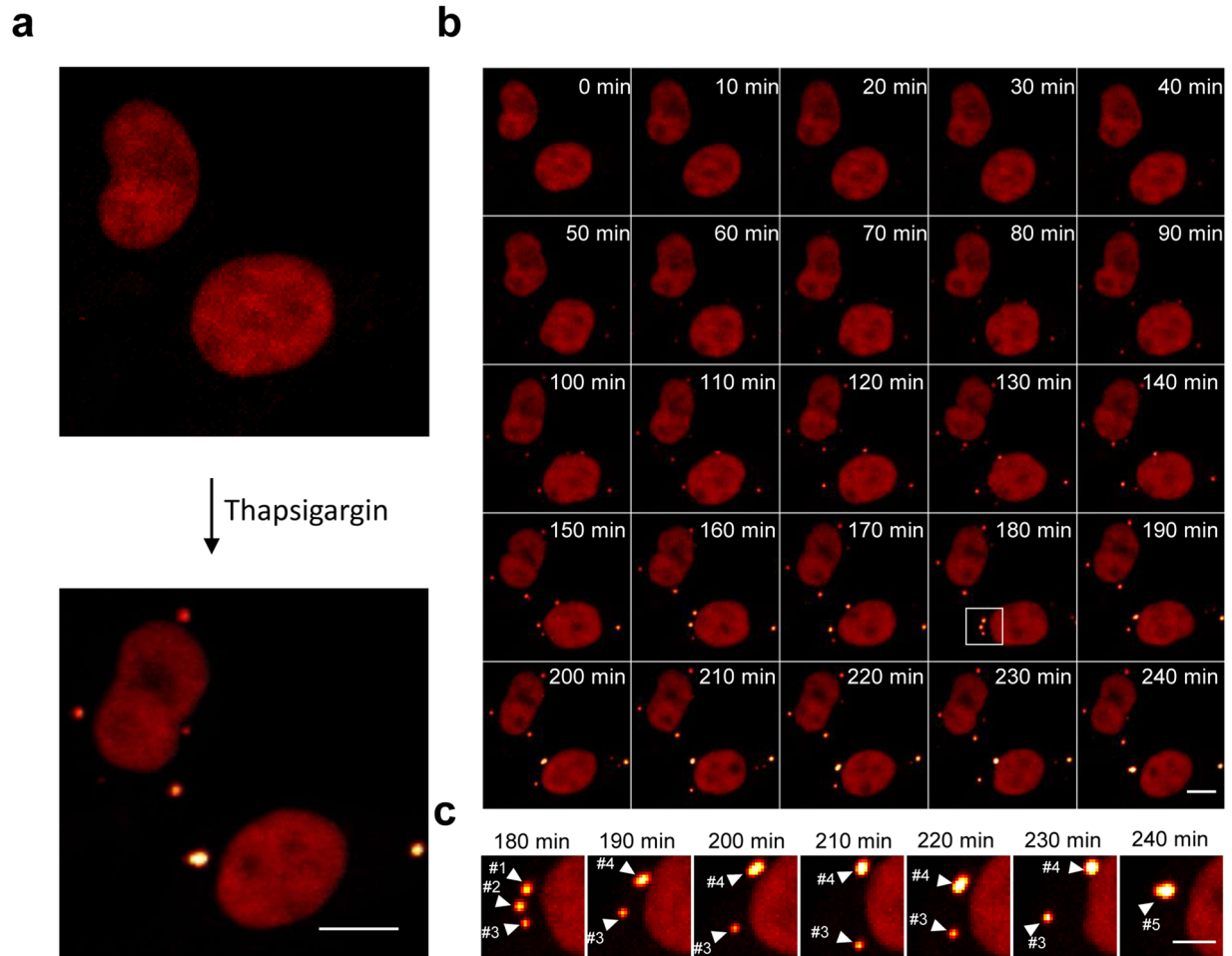


**Extended Data Fig. 6 | U-body puncta formation in HEK293T cells after thapsigargin induction. (a)** Thapsigargin-induced U-body formation. Scale bar, 10 μm. **(b)** HEK293T cells expressing U1-Clivia were treated with thapsigargin and consecutive imaging was taken every 10 min. Scale bar, 10 μm. **(c)** Zoom-in of the white square indicated region from **(b)** to show the fusion of small U-body puncta to form big U-body puncta. The # 1 and # 2 U-body puncta were fused to form the # 4 U-body punctum, and then the # 3 and # 4 U-body puncta were fused to form the # 5 U-body punctum. Scale bar, 5 μm.
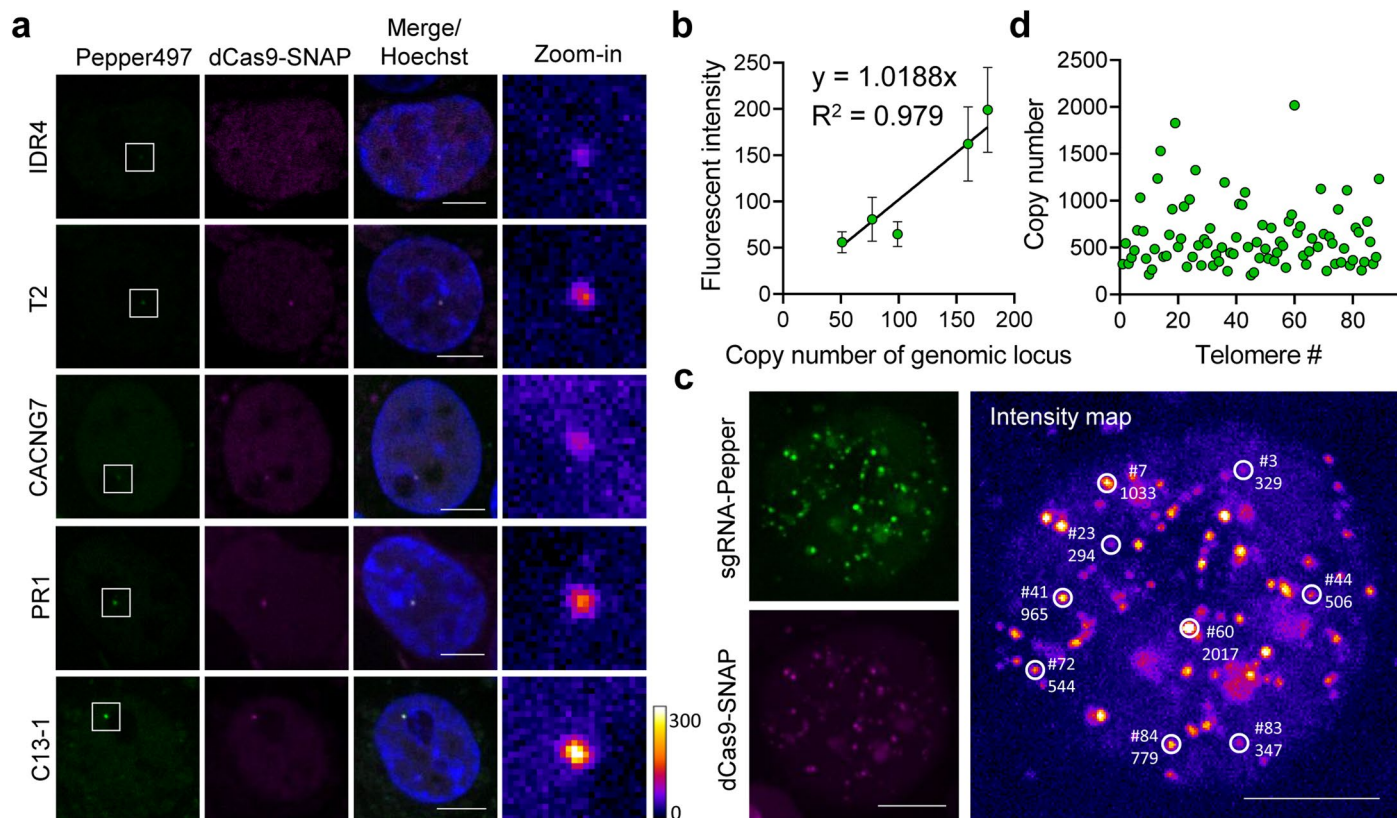
**Extended Data Fig. 7 | Determination of the telomere length based on signal intensity of Pepper-tagged sgRNA. (a)** Imaging of genomic foci with varied copy number by sgRNA-Pepper. Pepper-tagged sgRNAs targeting to genomic loci with varied copy number: C13-1 (177 copies) located in chromosome 13, PR1 (160 copies), CACNG7 (99 copies), T2 (77 copies) and IDR4 (51 copies) located in chromosome 19 were constructed and used for genomic labeling. Zoom-in of the white square indicated regions was shown. Scale bars, 5 μm. **(b)** The standard curve by plotting the fluorescent intensities on the x-axis and the copy number of genomic locus on the y-axis. The data were fit to a linear equation and the $R^2$ value was calculated. Data represent the mean ± s.d. (n = 10 cells). **(c)** Quantification analysis of the copy number of telomeres in a HEK293T cells. Scale bars, 5 μm. **(d)** Calculation of the copy number of telomeres from their fluorescent signals based on the equation in **(c)**.
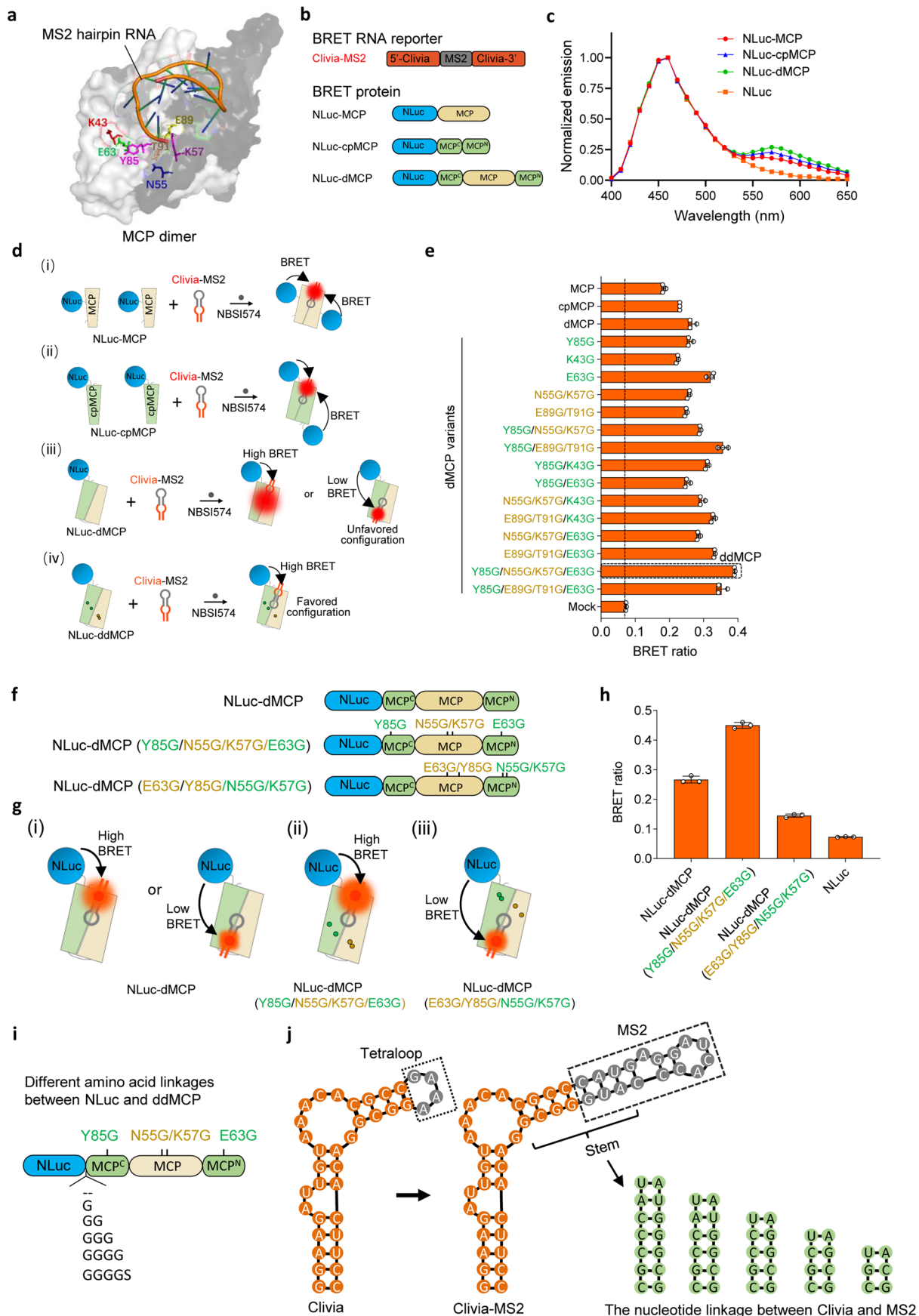
**Extended Data Fig. 8 | See next page for caption.**

**Extended Data Fig. 8 | The effect of different configurations of MS2-MCP complex on the BRET efficiencies. (a)** Structure information showing the interaction between MCP coat protein and MS2 hairpin RNA (PDB: 2C50). Amino acids in MCP protein dimer that participate in the binding of MS2 RNA are shown. **(b)** Schematic representation of the RNA reporter and BRET fusion proteins. **(c)** Emission spectra measurement of HEK293T cells expressing Clivia-MS2 and NLuc fusions upon incubation with 1 µM NBSI574 and 10 µM furimazine. Cells expressing Clivia-MS2 and NLuc without fusion with MCP were used as the control. Data were normalized to the maximal emission. **(d)** Schematic representation of the binding models of different BRET fusion proteins to Clivia-MS2 reporter RNA. **(e)** BRET efficiency for different BRET fusion proteins. HEK293T cells expressing Clivia-MS2 and different BRET fusion proteins were incubated with 1 µM NBSI574 and 10 µM furimazine, and the emission spectra were measured. The ratios of light intensity at the emission maximum of Clivia to that of NLuc were calculated. Cells expressing Clivia-MS2 and NLuc without fusion with M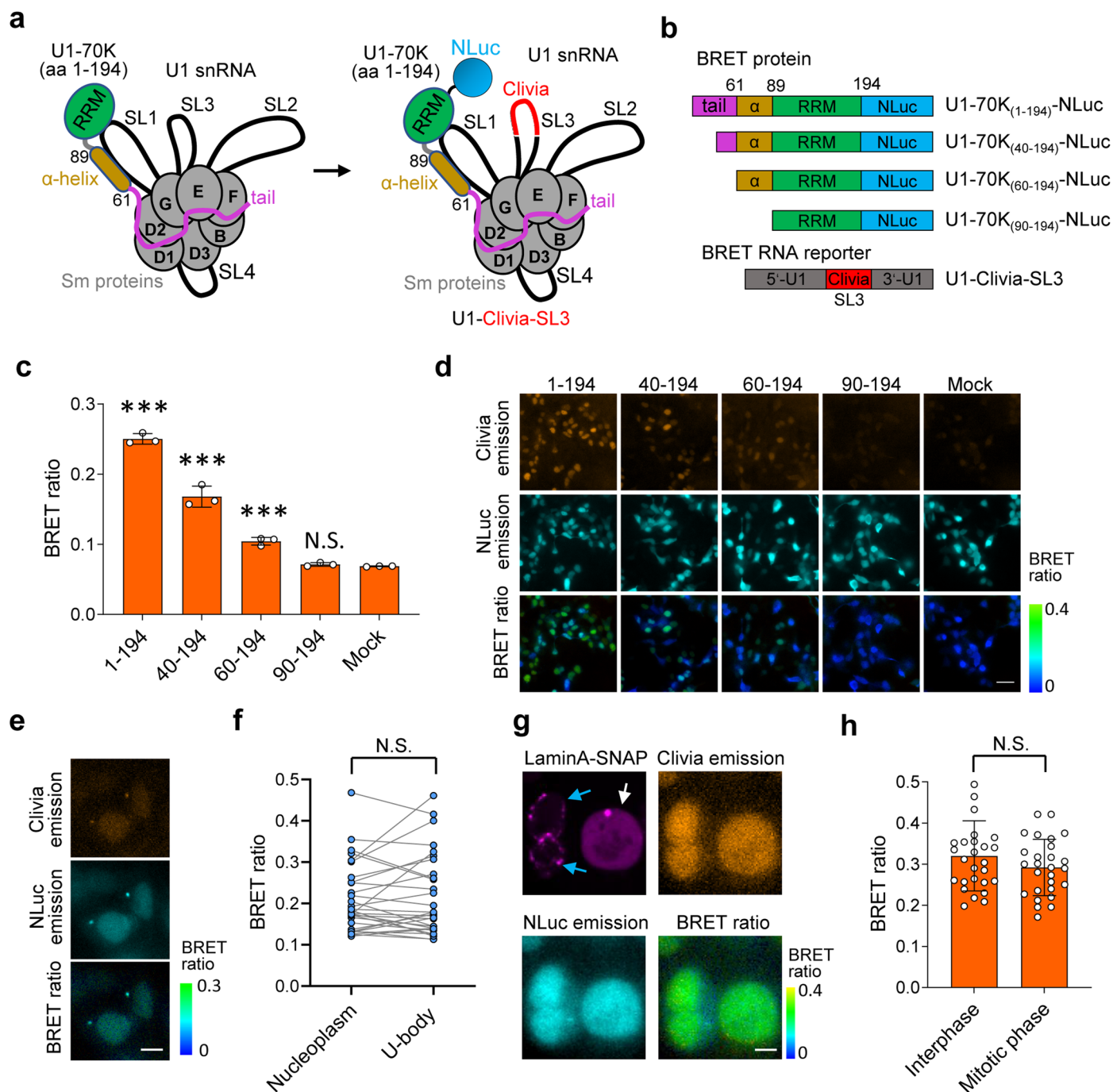CP were used as the controls. Data represent the mean ± s.d. from three biologically independent samples. **(f)** Schematic representation of the different BRET fusion proteins. **(g)** Schematic representation of the binding models of different BRET fusion proteins to Clivia-MS2 reporter RNA. In the first model, NLuc-dMCP can bind with Clivia-MS2 reporter RNA in two possible configurations and thus have different BRET efficiencies. In the second model, NLuc-dMCP (Y85G/N55G/K57G/E63G) contains the configuration-specific mutations in dMCP motif and may bind with MS2 reporter RNA in the configuration favored more efficient BRET. In the third model, NLuc-cpdMCP (N55G/K57G/E63G/Y85G) also contains the configuration-specific mutations in dMCP motif and may bind with MS2 reporter RNA in the unfavored configuration with less efficient BRET. **(h)** BRET efficiency for different BRET fusion proteins. Data represent the mean ± s.d. from three biologically independent replicates. **(i)** Schematic representation of NLuc-ddMCP fusions containing different lengths of amino acid linkage between NLuc and ddMCP. **(j)** Schematic representation of the chimeric Clivia-MS2 reporter RNA containing different lengths of nucleotide stem between Clivia and MS2.
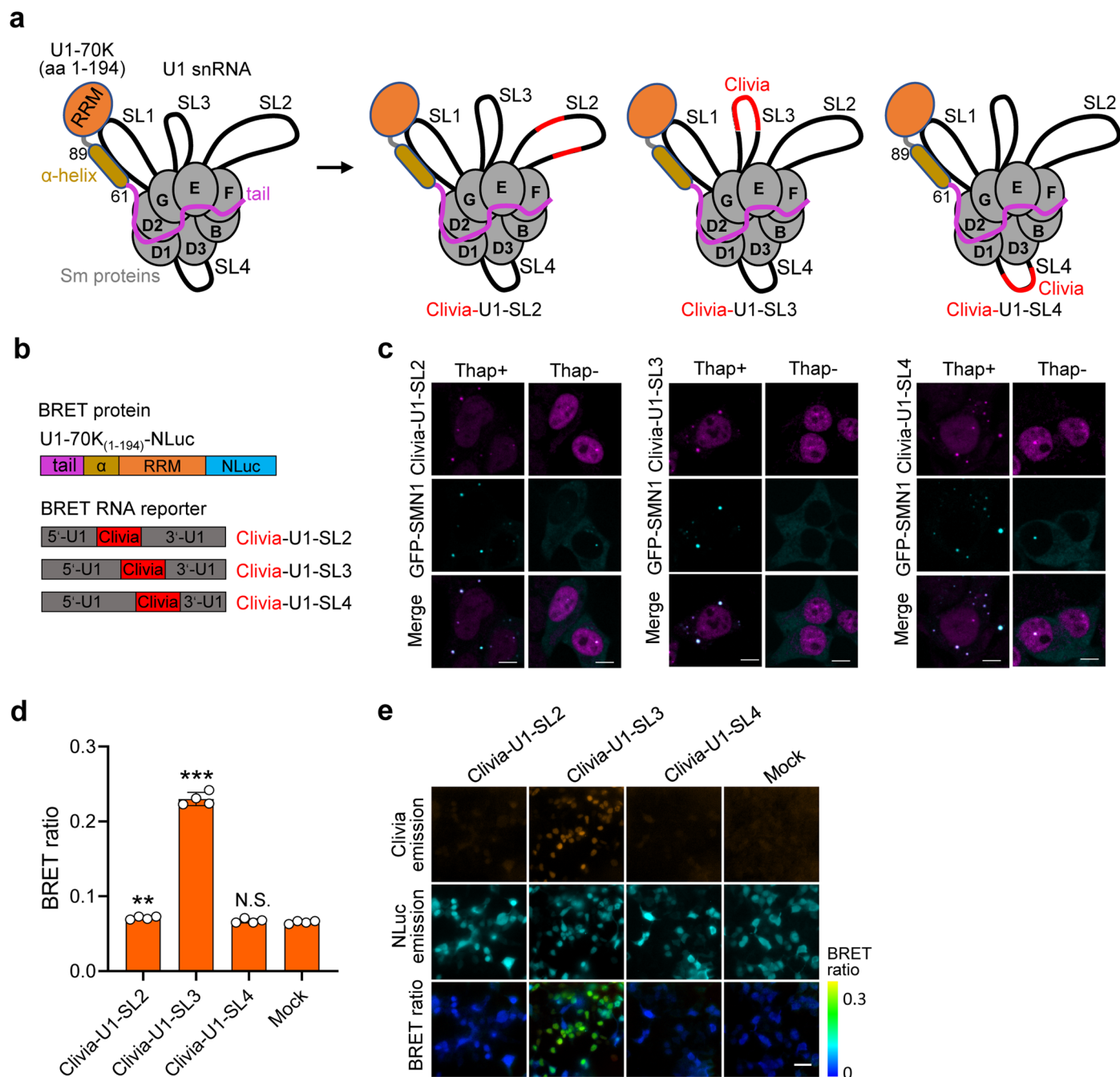
**Extended Data Fig. 9 | Detection of U1-70K and U1 snRNA interaction by the Clivia-based BRET system. (a)** Schematic illustration of different configurations of U1 snRNA with Clivia (red) insertion. **(b)** Schematic representation of different chimeric Clivia-U1 reporters and the fusion of NLuc and the RNA binding domain (amino acids 1-194) of U1-70K. **(c)** Validation of different chimeric Clivia-U1 reporter RNA for labeling of U-bodies induced by thapsigargin. Scale bars, 10 μm. **(d)** The BRET efficiency between U1-70K$_{(1-194)}$-NLuc and different chimeric Clivia-U1 RNA reporters. Cells expressing U1-70K$_{(1-194)}$-NLuc and Clivia were used as the controls. Statistical comparison was performed by a two-tailed t-test. **$P < 0.01$ and ***$P < 0.001$ versus control cells. N.S., no significant difference. Data represent the mean ± s.d. from four biologically independent replicates. **(e)** Imaging of HEK293T cells expressing U1-70K$_{(1-194)}$-NLuc and different chimeric Clivia-U1 RNA reporters upon incubation with 1 μM NBSI574 and 10 μM furimazine. Cells expressing U1-70K$_{(1-194)}$-NLuc and Clivia were used as the controls. Scale bars, 40 μm.

**Extended Data Fig. 10 | Detection of U1-70K and U1 snRNA interaction in U-bodies and cells during interphase and mitotic phase. (a)** Schematic illustration of Clivia-based BRET system for detection of the interaction between U1-70K and U1 snRNA. **(b)** Schematic representation of the fusions of NLuc and different U1-70K truncations. **(c)** The BRET efficiencies between Clivia-U1-SL3 and different fusion proteins. Cells expressing Clivia-U1-SL3 and NLuc were used as the controls. Data represent the mean ± s.d. from three biologically independent replicates. **(d)** Imaging of HEK293T cells expressing Clivia-U1-SL3 and different fusion proteins upon incubation with 1 μM NBSI574 and 10 μM furimazine. Cells expressing Clivia-U1-SL3 and NLuc were used as the controls. Scale bars, 40 μm. **(e)** Imaging of the BRET signals in the nucleoplasm and U-bodies. Scale bars, 10 μm. **(f)** Quantification of the BRET ratios in the nucleoplasm and U-bodies. Data represent the mean ± s.d. (N = 30 cells). **(g)** Imaging of the BRET signals in the cells during interphase and mitotic phase. HEK293T cell were co-transfected with plasmids expressing Clivia-U1-SL3, U1-70K$_{(1-194)}$-NLuc and LaminA-SNAP. The cells were incubated with 1 μM NBSI574 and 0.2 μM SNAP-Cell 647-SiR 24 h after transfection. Then BRET imaging was performed after 10 μM furimazine was added. LaminA-SNAP was used to visualize the status of nuclear envelope to indicate the stage of the cell cycle. During mitosis, the nuclear envelope breaks apart in prometaphase and reforms in late mitosis. Blue arrows indicated the cells during interphase and white arrow indicated the cell during mitotic phase. Scale bars, 20 μm. **(h)** Quantification of the BRET ratios in the cells during interphase and mitotic phase. Data represent the mean ± s.d. (N = 20 cells). Statistical comparisons in **(c)**, **(f)** and **(h)** were performed by a two-tailed t-test. ***P < 0.001 versus control cells. N.S., no significant difference.

Corresponding author(s): Yi Yang

Last updated by author(s): Jul 12, 2023

# Reporting Summary

Nature Research wishes to improve the reproducibility of the work that we publish. This form provides structure for consistency and transparency in reporting. For further information on Nature Research policies, see our Editorial Policies and the Editorial Policy Checklist.

## Statistics

For all statistical analyses, confirm that the following items are present in the figure legend, table legend, main text, or Methods section.

| n/a | Confirmed | |
|---|---|---|
| ☐ | ☒ | The exact sample size ($n$) for each experimental group/condition, given as a discrete number and unit of measurement |
| ☐ | ☒ | A statement on whether measurements were taken from distinct samples or whether the same sample was measured repeatedly |
| ☐ | ☒ | The statistical test(s) used AND whether they are one- or two-sided<br>*Only common tests should be described solely by name; describe more complex techniques in the Methods section.* |
| ☐ | ☒ | A description of all covariates tested |
| ☒ | ☐ | A description of any assumptions or corrections, such as tests of normality and adjustment for multiple comparisons |
| ☐ | ☒ | A full description of the statistical parameters including central tendency (e.g. means) or other basic estimates (e.g. regression coefficient) AND variation (e.g. standard deviation) or associated estimates of uncertainty (e.g. confidence intervals) |
| ☐ | ☒ | For null hypothesis testing, the test statistic (e.g. $F$, $t$, $r$) with confidence intervals, effect sizes, degrees of freedom and $P$ value noted<br>*Give P values as exact values whenever suitable.* |
| ☒ | ☐ | For Bayesian analysis, information on the choice of priors and Markov chain Monte Carlo settings |
| ☒ | ☐ | For hierarchical and complex designs, identification of the appropriate level for tests and full reporting of outcomes |
| ☒ | ☐ | Estimates of effect sizes (e.g. Cohen's $d$, Pearson's $r$), indicating how they were calculated |

*Our web collection on statistics for biologists contains articles on many of the points above.*

## Software and code

Policy information about availability of computer code

| | |
|---|---|
| Data collection | Live cell fluorescence imaging was performed using a Leica SP8 confocal laser scanning microscope equipped with a HC PL APO CS2 ×63.0/1.40 OIL objective, a HyD detector, or a Yokogawa CSU-W1 SoRa spinning disk confocal attached to an inverted Nikon(TI-E) microscope with Nikon Perfect Focus system, a Plan Apo VC 100×/1.40 Oil objective, a photometrics Prime 95B sCMOS camera, or Nikon N-SIM S super-resolution imaging microscope equipped with a SR HP Apo TIRF 100× (numerical aperture 1.49) OIL objective, a HAMAMATSU ORCA-Flash4.0 sCMOS camera. A CytoFLEX S flow cytometer was used for analysis of RNA labeling in E.coli cells. A Synergy 2 and a Neo2 multi-mode microplate reader (BioTek) were used to determine the in vitro properties of the RNA-fluorophore complexes. A qTower cycler (Analytik Jena AG) was used to collect the melting temperature of the RNA-fluorophore complexes. A 5200 Multi station (Tanon) was used for fluorescence imaging of the gel. An IVIS® Spectrum CT from PerkinElmer was used for mice imaging. |
| Data analysis | Leica Application Suite X 1.8.1, NIS-Elements AR 5.20.02, NIS-Elements AR 5.21.00 and ImageJ 1.49k were used to process the imaging data. Gen5™ Reader Control and Data Analysis Software2.0 was used to process microplate reader data. Cytexpert program 2.3.0.84 (Beckman Coulter) was used to process flow cytometry data. SigmaPlot 12.0 and Graphpad Prism 7.01 were used for data analysis. |

For manuscripts utilizing custom algorithms or software that are central to the research but not yet described in published literature, software must be made available to editors and reviewers. We strongly encourage code deposition in a community repository (e.g. GitHub). See the Nature Research guidelines for submitting code & software for further information.

## Data

The data supporting the findings of this study are available within the paper and its Supplementary Information files. Source data are provided in this paper.

# Field-specific reporting

Please select the one below that is the best fit for your research. If you are not sure, read the appropriate sections before making your selection.

☒ Life sciences  ☐ Behavioural & social sciences  ☐ Ecological, evolutionary & environmental sciences

For a reference copy of the document with all sections, see nature.com/documents/nr-reporting-summary-flat.pdf

# Life sciences study design

All studies must disclose on these points even when the disclosure is negative.

| | |
|---|---|
| Sample size | No statistical methods were used to pre-determine sample size. The sample size (n) of each experiment is provided in the figure/table legends in the main manuscript and supplementary information file. These sizes have previously been shown as sufficiently powered to determine statistical differences in mean values of our investigated parameters. |
| Data exclusions | No data was excluded from the analysis. |
| Replication | Each data in this manuscript is reliably reproduced. The replication number of each data is indicated in the legend of corresponding figures. |
| Randomization | Cells and mice were randomly assigned into control or experimental groups. |
| Blinding | No blinding was performed because no studies were deemed to be influenced by human interpretation. |

# Reporting for specific materials, systems and methods

We require information from authors about some types of materials, experimental systems and methods used in many studies. Here, indicate whether each material, system or method listed is relevant to your study. If you are not sure if a list item applies to your research, read the appropriate section before selecting a response.

### Materials & experimental systems

| n/a | Involved in the study |
|---|---|
| ☐ | ☒ Antibodies |
| ☐ | ☒ Eukaryotic cell lines |
| ☒ | ☐ Palaeontology and archaeology |
| ☐ | ☒ Animals and other organisms |
| ☒ | ☐ Human research participants |
| ☒ | ☐ Clinical data |
| ☒ | ☐ Dual use research of concern |

### Methods

| n/a | Involved in the study |
|---|---|
| ☒ | ☐ ChIP-seq |
| ☐ | ☒ Flow cytometry |
| ☒ | ☐ MRI-based neuroimaging |

## Antibodies

| | |
|---|---|
| Antibodies used | *Goat Anti-Mouse IgG H&L (Alexa Fluor® 488) (abcam, ab150113)<br>*Mouse Anti-SMN/Gemin 1 antibody [2B1](abcam, ab5831) |
| Validation | *Goat Anti-Mouse IgG H&L (Alexa Fluor® 488) (abcam, ab150113)<br>see: https://www.abcam.com/Goat-Mouse-IgG-HL-Alexa-Fluor-488-ab150113.html<br>*Mouse Anti-SMN/Gemin 1 antibody [2B1](abcam, ab5831).<br>see: https://www.abcam.com/smngemin-1-antibody-2b1-ab5831.html |

# Eukaryotic cell lines

Policy information about [cell lines](#)

| | |
|---|---|
| Cell line source(s) | HEK293T (GNHu44) and HeLa (TCHu187) were purchased from the Cell Bank of Chinese Academy. |
| Authentication | No cell lines were authenticated |
| Mycoplasma contamination | All cell lines have been tested negative for mycoplasma contamination by PCR methods |
| Commonly misidentified lines (See [ICLAC](#) register) | No commonly misidentified cell lines were used |

# Animals and other organisms

Policy information about [studies involving animals](#); [ARRIVE guidelines](#) recommended for reporting animal research

| | |
|---|---|
| Laboratory animals | Four-week-old male KM mice (Shanghai Jie Si Jie Laboratory Animal CO. LTD) were used for the animal experiments. |
| Wild animals | None |
| Field-collected samples | None |
| Ethics oversight | All procedures involving animals were approved by the Institutional Animal Care and Use Committee of Shanghai and were conducted in accordance with the National Research Council Guide for Care and Use of Laboratory Animals. |

Note that full information on the approval of the study protocol must also be provided in the manuscript.

# Flow Cytometry

## Plots

Confirm that:

☒ The axis labels state the marker and fluorochrome used (e.g. CD4-FITC).

☒ The axis scales are clearly visible. Include numbers along axes only for bottom left plot of group (a 'group' is an analysis of identical markers).

☒ All plots are contour plots with outliers or pseudocolor plots.

☒ A numerical value for number of cells or percentage (with statistics) is provided.

## Methodology

| | |
|---|---|
| Sample preparation | The bacteria cells were centrifuged at 4,000 rpm and resuspended with buffer containing 40 mM HEPES, pH 7.4, 125 mM KCl, 5 mM MgCl2 and 0.5 µM NBSI. |
| Instrument | A CytoFLEX S flow cytometer with a 561-nm laser for mCherry fluorescence analysis. |
| Software | Cytexpert program (Beckman Coulter) was used to process flow cytometry data. |
| Cell population abundance | All reported populations were greater than 10,000 cells. |
| Gating strategy | The gate was placed based on the BL21 Star™ (DE3) cells transformed with empty vector and incubated with 0.5 µM NBSI to determine population fraction that expressed tRNA-R8. |

☒ Tick this box to confirm that a figure exemplifying the gating strategy is provided in the Supplementary Information.